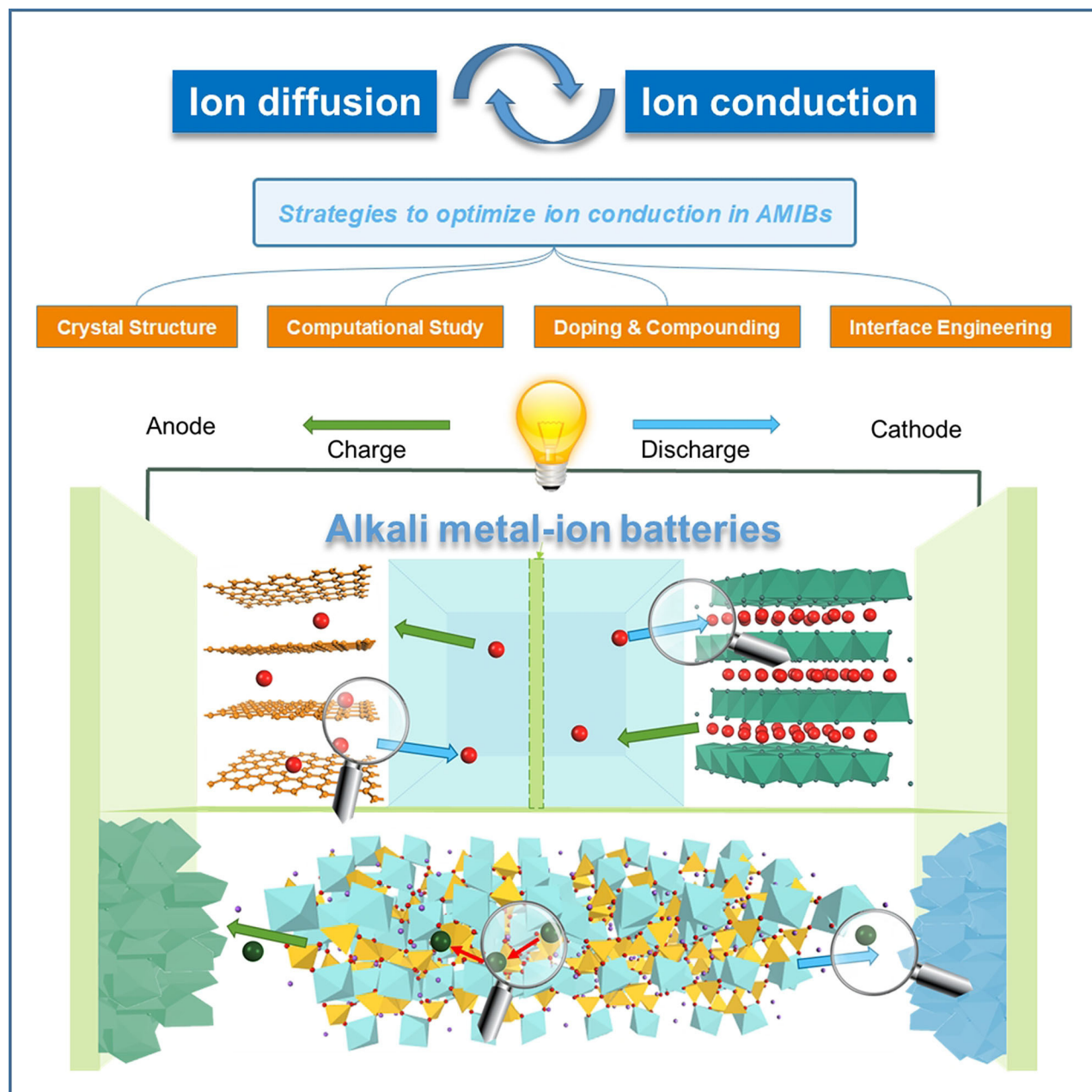


# Recent Research on Strategies to Improve Ion Conduction in Alkali Metal-Ion Batteries

TieLei Shao,<sup>[a]</sup> Chunyi Liu,<sup>[a]</sup> Wenjun Deng,<sup>[a]</sup> Chang Li,<sup>[a]</sup> Xusheng Wang,<sup>[b]</sup> Mianqi Xue,\*<sup>[b]</sup> and Rui Li\*<sup>[a]</sup>



Ion conduction refers to a conductive process consisting of the directional motion of ions driven by an electric field, which is one of the most important issues for further improvement of batteries in the current and foreseeable future. In order to better understand the conduction phenomena in alkali metal-ion ( $\text{Li}^+/\text{Na}^+/\text{K}^+$ ) batteries (AMIBs) and achieve technological breakthroughs, the recent studies on the ion diffusion of electrode materials and the ion conduction of electrolytes for

AMIBs are investigated. Three aspects of the factors that affecting ion conduction in AMIBs are mainly listed: (i) crystal structure related high ion conduction in crystalline materials. (ii) tuning the lattice volume and interface by doping and compounding. (iii) improvement in experimental synthesis and modification methods. Through this review, we hope to facilitate more efficient and targeted research to improve ion conduction in AMIBs.

## 1. Introduction

Rechargeable alkali metal-ion ( $\text{Li}^+/\text{Na}^+/\text{K}^+$ ) batteries (AMIBs) have achieved rapid success since their inception, benefiting from many advantages such as high discharge voltage, small size, and light weight.<sup>[1]</sup> Lithium-ion battery (LIB) is currently the most important alkali metal-ion battery, and it has one of the highest energy density among the energy storage technologies (Figure 1a).<sup>[2]</sup> LIB has been used in lightweight, flexible wearable

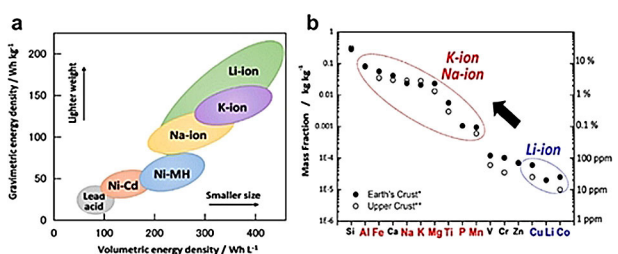


**Figure 1.** (a) Energy density of rechargeable batteries. (b) Abundance of elements in the Earth's crust.<sup>[2]</sup> Reprinted (adapted) with permission from ref. 2. Copyright (2018) John Wiley & Sons.

devices and transportation systems,<sup>[3]</sup> for example, smartphones, drones, hybrid and electric vehicles. In order to achieve better performance to meet higher requirements, people have developed and commercialized a variety of cathode materials such as  $\text{LiCoO}_2$ ,  $\text{LiMn}_2\text{O}_4$ ,  $\text{LiFePO}_4$ , ternary material NMC ( $\text{LiNi}_x\text{Co}_y\text{Mn}_z\text{O}_2$ ,  $x+y+z=1$ ).<sup>[4]</sup> At the same time, there are also many challenges in the design of the battery, such as better cycle performance, better safety, higher power density and energy density. However, due to the scarcity of lithium resources (accounting for 0.0017% of the crust, compared to 2.36% of sodium and 2.09% of potassium, respectively,<sup>[5]</sup> as shown in Figure 1b) and service life of LIB, there is an increasing amount of research activities focused on other rechargeable batteries (such as  $\text{Na}^+$ ,  $\text{K}^+$ ,  $\text{Mg}^{2+}$ ,  $\text{Al}^{3+}$ ,  $\text{Zn}^{2+}$ ) and supercapacitors (or

hybrid supercapacitors) as alternative energy-storage devices. On account of similar chemical properties, greater abundant reserves, and lower costs, the sodium-ion battery (SIB) and potassium-ion battery (PIB) have been perceived as reliable alternatives for the LIB<sup>[6]</sup>. It is generally believed that the significantly larger size of Na ion and K ion (102 pm and 138 pm, respectively, relative to 76 pm of Li ion) could be expected to mean higher migration barriers in the bottle-neck-constrained crystals (for example, the anion-close-packed olivine) and limit the energy density. Meanwhile, the further commercial applications of SIB and PIB present significant challenges due to the lack of corresponding electrode materials and narrow electrochemical windows in aqueous systems. Recent reports indicate that K ion has higher ionic conductivity in non-aqueous electrolytes<sup>[7]</sup> and a faster diffusion rate in carbon anode materials<sup>[8]</sup>. In order to better understand these issues, it is necessary to understand the ion conduction phenomenon and related influencing factors of the alkali metal ions in the corresponding battery materials.

Figure 2 shows a schematic diagram of charge and discharge process of a conventional lithium-ion battery (I) and a typical all-solid-state battery (II). The cathode material is a layered transition metal oxide  $\text{LiCoO}_2$  and the anode material is graphite in the conventional battery. The solid-state electrolyte is a NASICON-like  $\text{Na}_3\text{Zr}_2\text{Si}_2\text{PO}_{12}$ . During the charging process, Li/Na ions are removed from the cathode material, pass through the electrolyte, and enter the anode material. The

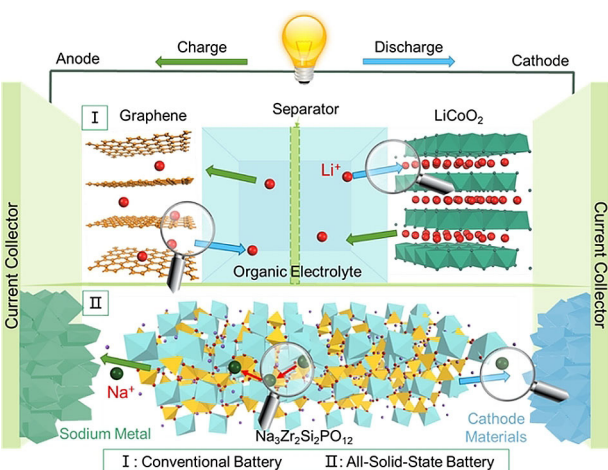


**Figure 2.** Schematic of the charging and discharging process in typical AMIBs.

- [a] T. Shao, C. Liu, W. Deng, C. Li, Prof. R. Li  
School of Advanced Materials  
Peking University Shenzhen Graduate School  
Shenzhen 518055 (China)  
E-mail: xuemeq@mail.ipc.ac.cn  
[b] Dr. X. Wang, Prof. M. Xue  
Technical Institute of Physics and Chemistry  
Chinese Academy of Sciences  
Beijing 100190 (China)  
E-mail: lirui@pkusz.edu.cn

discharge process is reversed. The insertion/extraction process of Li/Na ion is accompanied by the reduction/oxidation of a transition metal ion in the cathode material to accommodate the compensation gain/loss of an electron. In order to understand the conduction phenomena contained in it, the potential equation of the operating electrochemical cell was investigated,<sup>[9]</sup> and its mathematical expression is as follows:

$$E = E_0 - [(\eta_{ct})_a + (\eta_{ct})_c] - [(\eta_c)_a + (\eta_c)_c] - iR_i = iR \quad (1)$$

Where  $E$  is the operating voltage of the battery,  $E_0$  is the standard battery voltage,  $(\eta_{ct})_a$ ,  $(\eta_{ct})_c$  are the activation polarizations (charge-transfer over voltage) at the anode and cathode,  $(\eta_c)_a$ ,  $(\eta_c)_c$  are the concentration polarizations at the anode and cathode,  $i$  is the battery operating current,  $R_i$  is the internal resistance of the battery, and  $R$  is the apparent battery resistance. The internal resistance  $R_i$  of the battery is mainly derived from the transmission of ions and electrons in the three parts of the host crystal of the anode and cathode, the electrolyte, and the electrode-electrolyte interface (as shown by the magnifiers in Figure 2), and the activation and concen-

tration polarizations are related to the kinetics of charge transfer and mass transfer, respectively.<sup>[10]</sup> Poor ion transport in any part of the AMIBs can lead to a decrease in rate capability, actual capacity and cycle ability. So understanding the relationship between the generation of these internal resistances and ion conduction is significant to optimize battery performance.

The construction of theoretical models and the quantitative calculations of related parameters are indispensable to predict and improve the performance of battery materials. With the help of the first-principle calculation based on density functional theory (DFT), combined with molecular dynamics (MD) simulation and Monte Carlo (MC) methods, a lot of studies about computational simulation and core problems of battery materials at the atomic scale have been carried out,<sup>[11]</sup> and many breakthroughs have also been achieved in material design, synthesis, simulation calculations and evaluation. These have led to updated understandings in many aspects, such as the evolution of ions in the process of charge and discharge of electrode materials,<sup>[11d,12]</sup> diffusion kinetics in electrode materials,<sup>[13]</sup> growth mechanism of SEI, relationship between potential



Tielei Shao is now a master student in Advanced Materials at Peking University. He received his Bachelor (2016) degrees in Mechanical engineering from Tsinghua University, China. His research is focused on aqueous rechargeable metal-ion batteries for advanced energy storage systems. His primary interests are understanding the effect of structure, composition and morphology on electrochemical performance.



Chunyi Liu is now a master student in Advanced Materials at Peking University. She received her Bachelor (2016) degrees in Chemistry from Peking University, China. Her research is focused on aqueous rechargeable metal-ion batteries for advanced energy storage systems. Her primary interests are hybrid battery devices based on mixed-ion electrolytes.



Wenjun Deng is now a research assistant of School of Advanced Materials, Peking University Shenzhen Graduate School. He received his Bachelor (2009) and Master (2012) degree in School of Science from Nanchang University. His research interests include lithium-ion batteries and supercapacitors.



Chang Li is now a master student in Advanced Materials at Peking University. He received his Bachelor (2016) degrees from Central South University, China. His research is focused on aqueous rechargeable metal-ion batteries for advanced energy storage systems. His primary interests are aqueous potassium-ion battery devices.



Xusheng Wang is now a research fellow at Technical Institute of Physics and Chemistry, Chinese Academy of Sciences, Beijing, China. He obtained his Ph.D. degree in College of Chemistry and Molecular Engineering at Peking University, China, in 2018. His research interests include electrode materials, electrolytes, and reactions of various types of secondary ion batteries (lithium-, sodium-, magnesium-ion batteries, etc.).



Mianqi Xue is now a professor in Technical Institute of Physics and Chemistry, Chinese Academy of Sciences. He obtained his Bachelor degree in Materials Chemistry from Jinan University in 2005 and Ph.D. in Chemistry from Renmin University of China in 2012. His work is devoted to ordered conducting polymer system and their application such as secondary ion batteries.



Rui Li is now an associate professor in the School of Advanced Materials at Peking University. He received his BE and PhD in Materials Science from Zhejiang University in 2001 and 2007, respectively. His research interests focus on materials for electrochemical energy storage devices, especially secondary batteries and supercapacitors.

and structure, and space charge layer distribution. Through the combination of theoretical calculations and experiments, the key scientific issues that current researchers expect to solve include: (1) To find electrolyte materials with higher ionic conductivity through simulation and experiment. (2) To understand the complex conduction process associated with battery reactions, such as diffusion mechanism, defect effects, interface problems and size effects. (3) To understand the relationship between the macroscopic performance and the microstructure of the battery. (4) To develop new battery systems.

In this review, we focused on the ion conduction associated with the above problems of the AMIBs to explore the key influencing factors and the recent improvement strategies. This review will be presented in the following order: First, in the section 2, the fundamentals of ion conduction in both liquids and solid conductors are introduced, as well as its specific influencing factors. Well-known methods for calculating transmission parameters in ion conduction processes are also compared, as well as related simulation methods (such as DFT, MD) and their applications. Then, in the section 3, the research on ion conduction reported in the past three years are mainly studied, which includes: (i) The investigation of the ionic diffusivity in the electrode and the ionic conductivity in the electrolyte of the AMIBs. (ii) The latest computational studies and research hotspots. (iii) The recent strategies to improve ion conduction, which also includes three parts: a. The effect of crystal structure on ion conduction mechanism and performance. b. The effect of doping and compounding on lattice volume and interface. c. Recently improvement in experimental synthesis and modification methods. Finally, we expect that by summarizing these strategies of ion conduction to predict possible future development trends and help its further development in the future.

## 2. Fundamentals and Theoretical Methods in Alkali Metal-Ion Batteries

In this section, the related research and fundamentals of ion conduction phenomena are introduced. Related experimental methods for calculating ionic conductivity are investigated, as well as first-principles calculations and molecular dynamics studies involving with ion conduction. It should be noted that this is the basic physicochemical knowledge that has been

reported many times, and the description are maintained as the original literature.

### 2.1. Fundamentals of Ion Conduction

Ion conduction is a key indicator of battery performance because it quantifies the available extent which ions move to the ongoing electrochemical reaction, and it also determines the output power density of the battery. The ion conduction in AMIBs mainly includes conduction of ions in liquid electrolytes and solid conductors, further subdivided, the liquid electrolytes include protic solvent electrolytes and aprotic solvent electrolytes. Solid conductors include electrode materials and solid-state electrolytes (SSE), which can be further subdivided into Solid Polymer Electrolytes (SPE), Superionic Crystalline Electrolytes (SCE), Superionic Glassy Electrolytes (SGE) and their mixtures. Here, we mainly discuss the ion conduction mechanism and related influencing factors of alkali metal ions in electrode materials and electrolytes (aprotic solvent electrolytes and solid-state electrolytes). Due to the differences in physical properties between liquid and solid, it is clear that the ion conduction mechanisms of the both are also significantly different.

#### 2.1.1. Ion Conduction in Aprotic Solvent Electrolytes

It generally has a high ionic conductivity (about  $10^{-3}$  to  $10^{-2}$  S/cm) over a wide temperature range for ion transport in an aprotic solvent electrolyte. Its transport process begins with the solvation and dissociation of ionic compounds (usually crystalline salts) by polar solvent molecules, which then migrate and diffuse through the solvent medium. Therefore, the ideal solvent should satisfy a higher dielectric constant (to dissolve the salt) and a lower viscosity (to increase the ion mobility) while still meeting the interface stability requirements of the anode and cathode.<sup>[14]</sup> In order to better understand the influencing factors, the relevant equations and explanations of the ion conduction in aprotic solvent electrolytes are shown in Table 1.<sup>[15]</sup>

The relationship among the ionic conductivity  $\sigma$ , the number of free ions  $n_i$  and the ion mobility  $u_i$  is as shown in Table 1-Equation 1, and the ionic conductivity  $\sigma$  is proportional to the number of free ions  $n_i$  and the ion mobility  $u_i$ . The ion mobility  $u_i$  indicates the degree of difficulty for the ion to pass

**Table 1.** Equations related to the ion conduction in aprotic solvent electrolytes.<sup>[15a,d,16–17]</sup>

NO.	Title	Equation	Comments
1	Ionic conductivity in liquid	$\sigma = \sum_i n_i u_i Z_i e$	• $n_i$ – the free ion number; $u_i$ – ionic mobility • $Z_i$ – the valence order of ionic species $i$ ; $e$ – the unit charge of electrons
2	Nernst-Planck relationship	$D_i = u_i K_B T$	• the relationship of diffusivity and mobility; $K_B$ – Boltzmann constant
3	Einstein-Stokes relation	$D_i = \frac{K_B T}{6\pi\eta R_0}$	• $\eta$ – viscosity of the medium; $R_0$ – radius of sphere (particle)
4	Arrhenius equation	$K = A \exp(-\frac{E_A}{K_B T})$	• $A$ – pre-exponential factor; $E_A$ – the activation energy
5	Vogel-Tamman-Fulcher equation	$\sigma = AT^{-1/2}e^{-B/(T-T_0)}$	• $A/B$ – constants characteristic of the conduction process • $T_0$ – the vanishing conductivity temperature

through the medium when an external electric field is applied. In contrast, the ion diffusivity  $D_i$  indicates the degree of difficulty for the ion to pass through the medium under the concentration gradient. The relationship between  $D_i$  and  $u_i$  is expressed by the Nernst-Planck relationship (Table 1-Equation 2). Combining the Equation 1&2, the relationship between the ionic conductivity  $\sigma$  and the ionic diffusivity  $D_i$  can be obtained. Calculating the ion mobility  $u_i$  can also obtain several parameters such as ion migration velocity and ion flux, thereby further calculating current density, etc. For a particular alkali metal ion electrolyte, the only variable in salt structure is the anion. In a given nonaqueous solvent system, the dissociation of a lithium salt would be facilitated if the anion is well stabilized by electron-withdrawing functionalities, such as  $\text{PF}_6^-$ . On the other hand, the Einstein-Stokes relationship given by Table 1-Equation 3 shows that the diffusivity  $D_i$  of the ion changes inversely with its ionic radius  $R_0$ , where  $\eta$  is the viscosity of the medium and  $R_0$  is the radius of sphere (particle). It seems that the ion mobility  $u_i$  of a particular ion appears to be only related to the type of solvent used. However, it has also been reported<sup>[16]</sup> that an anion with a lower mobility can increase the migration number of cation, but it has a large impact<sup>[17]</sup> on the total ionic conductivity, so the method of improving ionic conduction by changing the type of salt has not been widely pursued. So far, there is no suitable single solvent to satisfy the above two conditions, so the usually employed method is to mix the solvents which have a high dielectric constant (such as Ethylene Carbonate EC) and a low viscosity (Dimethyl Carbonate DMC, Ethyl Methyl Carbonate EMC, etc.) to form a binary or polybasic solvent. But this also increases the complexity of optimizing ionic conductivity. Schweiger et al.<sup>[18]</sup> developed an algorithm that allows one to rapidly locate conductivity maxima in such complicated environments. Compared to the "interpolation method",<sup>[19]</sup> the time and sample size are significantly reduced.

In addition to the composition of the solvent, the concentration of the salt and the temperature of the solvent are also important factors affecting the dielectric constant and viscosity.<sup>[19–20]</sup> At low salt concentrations (<1.0 M), the number of free ions increases with salt concentration, consequently, ion conductivity also increases until it peaks at a higher concentration, and any increase in salt concentration results in higher ion aggregation and higher viscosity of the solution after this peak, which reduces both the free ion number and the ionic mobility simultaneously. The effect of temperature on ionic

conductivity is similar to the concentration, it increases with temperature monotonically until a very high temperature where the dielectric constant outweighs the viscosity in affecting ion conduction. In order to understand the effect of temperature on ion conduction more clearly, the logarithmic molal conductivity is plotted against the inverse of temperature. The results show that, unlike the Arrhenius type (Table 1-Equation 4), the effect of temperature on ion conduction in aprotic liquids fits well with the Vogel-Tamman-Fulcher (VTF) equation (Table 1-Equation 5).

There are also differences in the ion conduction of different alkali metal ions in the same solvent, which may come from their Lewis acidity. Since weaker Lewis acidity means weaker interaction of cations with the anions in electrolyte, alkali metal ion with larger ion radius usually possesses smaller Stokes' radius of solvated ions and lower activation energy at interfaces. Stokes' radii are 4.8, 4.6 and 4.5 Å<sup>[21]</sup> and desolvation energy are 215.8, 158.2 and 119.1 KJ mol<sup>-1</sup> for  $\text{Li}^+$ ,  $\text{Na}^+$  and  $\text{K}^+$  in PC, respectively.<sup>[22]</sup> In this way, ionic conductivity of  $\text{K}^+$  and  $\text{Na}^+$  are usually larger than that of  $\text{Li}^+$  due to the synergistic effect of smaller Stokes' radii and lower activation energy. As recently reported by Komaba et al.<sup>[22]</sup> in the concentration range from 0.5 to 2.0 mol dm<sup>-3</sup>, ionic conductivities for  $\text{LiN}(\text{SO}_2\text{F})_2$ , ( $\text{LiFSA}$ ),  $\text{NaN}(\text{SO}_2\text{F})_2$  ( $\text{NaFSA}$ ) and  $\text{KN}(\text{SO}_2\text{F})_2$  ( $\text{KFSA}$ ) are in order of  $\text{LiFSA} < \text{NaFSA} < \text{KFSA}$  in PC. Furthermore, it has been evidenced that transference number of  $\text{Na}^+$  is higher than that of  $\text{Li}^+$  for  $\text{MPF}_6^-$  ( $M = \text{Li}$  or  $\text{Na}$ ) in EC:DEC (=1:1 v/v) solution.<sup>[22]</sup>

### 2.1.2. Ion Conduction in Solid Conductors

To understand the concept of ion conduction in solid conductors, it is important to study the diffusion properties of ions, which determine the key performance indicators of alkali metal-ion batteries, such as charge and discharge rate, practical capacity and cycling stability. The relevant equations and descriptions of ion conduction in solid conductors are shown in Table 2.<sup>[9,16,23]</sup>

The governing equation used to describe the diffusion process is known as Fick's law<sup>[16,23]</sup> (Table 2-Equation 1), where  $j_i$  is the ion flux and  $D_i$  is the diffusivity. It describes the law of ion flux vs concentration gradients and concentration vs time. In solid conductors, diffusion is achieved by random migration of particles that resulting in exchange with adjacent sites. Unlike the rapid exchange of solvated molecules and solvent mole-

**Table 2.** Equations related to the ion conduction in solid conductors.<sup>[9,16,23]</sup>

NO.	Title	Equation	Comments
1	Fick's law	$j_i = -D_i \nabla c_i$ $\& \frac{\partial c}{\partial t} = \nabla \cdot (D \nabla c_i)$	• $j_i$ – the ion flux; $\nabla c_i$ – concentration gradient
2	Diffusivity in solid	$D_i = a_i^2 \cdot \nu^0 \exp(-\frac{E_A}{k_B T})$	• $a_i$ – the jump length • $\nu^0$ – attempt frequency of the order of Debye frequency of the lattice
3	Temperature dependence of diffusivity in solid	$D_i = D^0 \exp(-\frac{E_m}{k_B T})$	• $D^0$ – pre-exponential factor; $E_m$ – the migration energy • non-defect mediated interstitial diffusion
4	Temperature dependence of diffusivity in solid	$D_i = D^0 \exp(-\frac{E_m + E_f}{k_B T})$	• $E_f$ – Defect generation energy vacancy mediated diffusion
5	Ionic conductivity vs diffusivity.	$\sigma = \frac{q_i^2 c_i}{k_B T} \cdot D_i$	• $q_i$ – charge of solute 'i' ( $i = 1, 2$ ); $c_i$ – concentration of $i$

molecules in a homogeneous environment in the aprotic solvent electrolyte, the diffusion of mobile species in a crystalline solid needs to pass through periodic bottleneck points, which define an energetic barrier that greatly influences ionic mobility and ionic conductivity. It means low migration energies lead to high ionic mobility and conductivity.<sup>[24]</sup> Corresponding to the temperature dependence of the ionic diffusivity in the liquid (Stokes-Einstein relationship), the relationship between the ionic diffusivity and the temperature in the solid conductors is in accordance with Table 2-Equation 2, Where  $a_i$  is the jump distance and  $\nu^0$  is the trial frequency of the lattice.

In general, diffusion mechanisms in solid conductors can be classified into two categories: non-vacancy/non-defect mediated mechanisms, and vacancy/defect-mediated mechanisms.<sup>[23]</sup> The biggest difference is that the ions in the former are usually diffused by the dissolution of solute atoms at the gaps and substitution sites to form gaps or substituted solid solution, while the ions in the latter are usually diffused by the accumulated vacancies. The temperature dependence of the diffusivity in the two mechanisms corresponds to Table 2-Equation 3/4, where  $D^0$  is the pre-factor,  $E_m$  is the migration energy, and  $E_f$  is the defect generation energy. In addition, interstitials and vacancies can be created by substitution of aliovalent cations, whose formation energetics is governed by the trapping energy  $E_t$ .<sup>[24b]</sup> The apparent activation energy  $E_A$  of the ionic conductivity is composed of the migration energy  $E_m$  plus the defect generation energy  $E_f$  or the trapping energy  $E_t$ , so the activation energy of vacancy-mediated is higher than that of non-vacancy-mediated mechanism. When the defects in the crystal lattice are cationic vacancies and cation gaps, ion transport mainly occurs in the motion of the interstitial material, that is, non-vacancy/non-defect mediated, thus resulting higher ionic conductivity and lower activation enthalpy. So far, we have clarified the parameters related to the diffusivity  $D_i$ , and the relationship between the diffusivity  $D_i$  and the ionic conductivity  $\sigma$  is shown in Table 2-Equation 5, where  $q_i$  is the charge of each ion and  $c_i$  is the ion concentration. Since the ionic diffusivity  $D_i$  eliminates the influence of the difference in ion concentration  $c_i$  in different conductive media, it is also called normalized ionic conductivity.

In addition to the properties of the solid conductors mentioned above, both ion valence and size of the alkali metal ions themselves can greatly affect the ion conduction in the solid conductors.<sup>[25]</sup> As the electrostatic interactions between the mobile ions and the cations forming the structural skeleton increases, the activation energy of ion migration also increases significantly, resulting in both ionic conductivity and diffusivity decreasing with increasing ion valence.<sup>[26]</sup> In general, the dependence of the diffusivity on the ionic radius is not monotonic.<sup>[27]</sup> When the mobile ions are too small, they occupy sites with a large electrostatic trap, which contains closer near-neighboring counterions, resulting in high activation energy and slow diffusion. On the other hand, when the mobile ions are too large, the ions undergo greater resistance as they diffuse between the bottlenecks of the framework structure, and they also produce reduced diffusivity and large activation energy, thus the conduction of different alkali metal ions in the

same solid conductor is also different. For example, Nikitina et al.<sup>[28]</sup> calculated the diffusion and kinetic parameters of different alkali metal ions in KVPO<sub>4</sub>F by using Bond valence energy landscapes (BVEL). The result shows that all alkali metal positions are to be involved into the diffusion process. The migration network dimensionality varies depending on the nature of the alkali metal: from 3D in case of Li to 2D and 1D for Na and K respectively (shown as Figure 3). The Li<sup>+</sup> migration

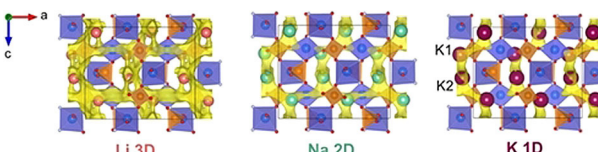


**Figure 3.** The ball-polyhedral representation of the KVPO<sub>4</sub>F crystal structure and the visualization of alkali ion migration pathways as bond valence energy isosurfaces. VO<sub>4</sub>F<sub>2</sub> are depicted as blue octahedra, PO<sub>4</sub> – dark-orange tetrahedra, oxygen and fluorine atoms – red and gray spheres respectively.<sup>[28]</sup> Reprinted (adapted) with permission from ref. 28. Copyright (2017) Electrochemical Society.

map comprises all three geometrically accessible channels along the a, b and c axes. Na<sup>+</sup> ions seem to follow a two-dimensional pathway in the (010) plane while K<sup>+</sup> ions exhibit a curved one-dimensional diffusion profile along the [001] direction of c axis.

## 2.2. Calculation and Simulation Methods

With the development of basic theoretical research and computer technology, many advanced experimental test methods have been applied in the field of energy storage in recent decades.<sup>[11b]</sup> However, many of the basic scientific issues involved are still unclear. Due to the errors and limitations in the experimental test, many problems such as the relationship between potential and structure, the space charge layer distribution cannot be clearly explained. Theoretical calculations and simulations can verify experimental results and guide the development of energy storage materials. Below, several commonly used methods for calculating the ionic diffusivity, as well as related simulation methods and their applications in the field of energy storage are introduced.

### 2.2.1. Methods for Calculating Ionic Diffusivity

In the previous section, the mutual conversion relationship between ionic conductivity and diffusivity in liquids and solid conductors and their calculation equations are introduced, the conversion between these two parameters can be achieved by calculation. The ionic diffusivity  $D_i$  is used as the main descriptive parameter for ion motion as well as describing the dynamic properties of materials. Here, different methods for measuring ionic diffusivity are mainly introduced: Cyclic Voltammetry (CV), Electrochemical Impedance Spectroscopy

(EIS), Potentiostatic Intermittent Titration Technique (PITT), Galvanostatic Intermittent Titration Technique (GITT), and Potential Relax Technique (PRT). The equations and related parameters<sup>[29]</sup> are shown in Table 3.

The basic principle of most electrochemical techniques is to drive the system away from the balance by manipulating the current or voltage while recording the other response. The collected data is then analyzed by using the appropriate physical model to obtain the required parameters. The derivation process of the test methods listed in Table 3 is inseparable from Fick's first & second law and Nernst equation. The difference is that different test methods use different boundary, initial conditions and numerical analysis methods, which is determined by the disturbance signal.<sup>[30]</sup> In general, each electrochemical technique has its own advantages and disadvantages. For example, The CV uses simple equipment and data processing is easy, but it can only obtain the apparent chemical diffusivity. The EIS method can be used to visually see whether the reaction is controlled by diffusion, but also only the apparent diffusivity can be obtained, and the molar volume  $V_M$  of the measured system is required to hardly change. Both the PITT and PRT only need to measure the thickness  $L$  of the electrode active material, avoiding the change of the active area  $A$  and the molar volume  $V_M$  of the electrode. The GITT combines transient and equilibrium measurements, in addition to the ionic diffusivity, a range of kinetic and thermodynamic properties are available, including partial conductivity, thermodynamic enhancement factors, stoichiometric open circuit voltage, and free formation energy etc. Compared to PITT, the GITT can eliminate the disturbance of resistance polarization (for example, ohmic resistance and charge transfer resistance) as long as these polarizations are fixed. Due to these differences, the choice of test method needs to be based on actual needs, combining multiple test methods to understand the electrochemical process is also a common approach.

In addition to the electrochemical techniques mentioned above, other test methods are also used, such as the Potential Step Chronoamperometry (PSCA),<sup>[31]</sup> which has the same equation expression as PITT, Current Pulse Relaxation (CPR)<sup>[32]</sup> similar to GITT, Radio of Potentio-charge capacity to Galvano-charge capacity (RPG), Capacity Intermittent Titration Technique (CITT) and so on. It has been reported that a 4-electrode system is used to measure the diffusion coefficient of particles in a medium by detecting the time that particles pass through the medium.<sup>[33]</sup>

### 2.2.2. Methods for Computational Studies

In recent years, First-Principles Calculations which based on Density Functional Theory (DFT), combined with Molecular Dynamics (MD) and Monte Carlo (MC) methods, have made many breakthroughs in material design, synthesis, simulation calculation and evaluation. These methods have become important foundation and core technologies for material calculation simulation on the atomic scale. This section will focus on some of the key knowledge and applications of First-Principles Calculations, Molecular Dynamics and other material simulation methods.

#### 2.2.2.1. First-Principles Calculations Based on DFT

Without introducing any empirical parameters, the method of calculating the Schrödinger equation by calculating the relevant physical parameters through known quantum mechanics theory and Combined with mathematical tools to calculate the basic properties of the ground-state material is called "first-principles calculation".<sup>[34]</sup> Involved approximations, equations and theories are listed in Table 4 for better understanding.<sup>[33–35]</sup>

**Table 3.** Analytical Equations for Calculating the Chemical Diffusion Coefficient of CV, EIS, PITT, GITT and PRT.<sup>[29]</sup>

Methods	$t \ll L^2/D_i$	$t \gg L^2/D_i$
CV	$D_i = \left( \frac{dI_p}{dv} / 0.446nFAC_i f^{1/2} \right)^2$ • $I_p$ – peak current during CV scan ; $v$ - scan rate • $n$ – number of electrons involved in the redox reaction; $A$ - electrochemical active area • $C_i$ – initial concentration of $i$ ; $f = \frac{nF}{RT}$ ; $F$ - Faraday constant	
EIS	$D_i = \frac{1}{2} \left[ \frac{V_M}{Z_i FA B} \frac{dE(\delta)}{d\delta} \right]^2$ • $Z_i$ – the charge number of electroactive species $i$ ; $B$ – Warburg factor • $V_M$ – the molar volume of the electrode material; $E(\delta)$ – the steady-state equilibrium voltage (i.e., open circuit voltage) • $L$ – the characteristic length of the electrode material; $\text{Re}(Z_d)$ - the real part of the diffusion impedance	$D_i = \frac{V_M L}{3FA\text{Re}(Z_d)} \frac{dE(\delta)}{d\delta}$
PITT	$D_i = L^2 \pi \left( \frac{I(t)/t}{\Delta E} \frac{dE(\delta)}{d\delta} \right)^2$ • $I(t)$ – transient current during the voltage step; $\Delta E$ – magnitude of the voltage step; $\frac{d\ln(I/t)}{dt}$ – slope of the plot of $\ln(I/t)$ vs $t$	$D_i = - \frac{d\ln(I/t)}{dt} \frac{4L^2}{\pi^2}$
GITT	$D_i = \frac{4}{\pi} \left( \frac{V_M}{Z_i FA} \right)^2 \left[ \frac{dE(\delta)}{d\delta} / \frac{dE(t)}{dt} \right]^2$ • $I$ – the applied constant current • $E(t)$ – the transient voltage response of the working electrode during the constant current interval	$D_i = \frac{4L V_M}{3Z_i FA} \frac{dE(\delta)}{d\delta} \frac{1}{E(t) _{t=0} - E(t=0)}$
PRT	$D_i = \frac{L^2}{t\pi^2} \ln \left[ \frac{\exp\left(\frac{t-\tau_0}{R}\varphi_\infty F\right) - 1}{N} \right]$ • $t$ – time when the potential reaches equilibrium; $\varphi_\infty$ – the Balance electrode potential; $\varphi_0$ – the initial potential	

Note: The same symbols mentioned above have the same meanings and the specific key assumptions involved in each equation are no longer listed here.

**Table 4.** The fundamentals of First-Principles Calculations based on Density Functional Theory.<sup>[33–35]</sup>

Title	Descriptions or Equations
Adiabatic approximation	<ul style="list-style-type: none"> <li>Separate the motion of the nucleus and electrons to simplify the Schrödinger equation as follow:  <math>H = T_e + V_{ee} + \sum_j \nu(\vec{r}_j) T_n</math> - Electrokinetic energy; <math>V_{ee}</math> - Coulomb interaction between electrons; <math>\sum_j \nu(\vec{r}_j)</math> - Coulomb interaction between electrons and nuclei</li> </ul>
Hartree-Fock approximation	<ul style="list-style-type: none"> <li>The motion characteristics of a single electron depend only on the average density distribution of other electrons, but not on the instantaneous position</li> </ul>
Hohenberg-Kohn theorem	<ul style="list-style-type: none"> <li>Simplify complex multibody problems into self-consistent single-particle models with two basic assumptions</li> </ul>
Kohn-Sham equation	<ul style="list-style-type: none"> <li><math>[-\nabla^2 + V_{KS}[\rho(r)]]\varphi_i(r) = E_i \varphi_i(r)</math> <math>V_{KS}[\rho] = \nu(r) + \int d\mathbf{r}' \frac{\rho(\mathbf{r}')}{ \mathbf{r}-\mathbf{r}' } + \frac{\delta E_{xc}(\rho)}{\delta \rho(\mathbf{r})}</math></li> <li><math>\rho(r) = \sum_{i=1}^N  \varphi_i(r) ^2</math> Introducing the DFT to practical applications</li> </ul>
Local Density Approximation & Generalized Gradient Approximation	<ul style="list-style-type: none"> <li>By fitting the results of the system that has been accurately solved, the exchange correlation potential is expressed in a parametric form. LDA tends to over-localize the system description, while GGA is too delocalized</li> </ul>
Self-Consistent Field	<ul style="list-style-type: none"> <li>The results are converged by cyclic iteration, and the total energy and charge density distribution of the system are further calculated.</li> </ul>

Under the premise of the Born-Oppenheimer adiabatic approximation, the Self-Consistent Field (SCF) method is used to solve the Hartree-Fock (HF) equation and the Kohn-Sham (KS) equation, respectively. The essential difference between the two methods is as follows: by solving the system wave function to obtain other phase properties is HF method, and by calculating the system charge density to obtain other related properties is DFT method. For the HF method calculation, the electron wave function and its energy are obtained by the self-consistent field method. By adjusting the coefficients of a set of basic functions (single particles), the total electron energy of the system is minimized. Furthermore, the HF method reduces the error caused by the single electron approximation process by introducing a multi-column wavelet function, but it cannot be done in the DFT method unless it is processed by finding a more accurate density function. Based on the convenience of the semi-empirical calculation method, the DFT method can save the calculation time to the utmost extent. Moreover, the DFT method is more suitable for the theoretical study of molecular systems with transition metal elements and higher precision. Because of the consideration of electronic correlation, it is considered to be a more formal first-principle calculation method. In general, the first principle calculation in the DFT framework is implemented by the Vienna *ab-initio* package (VASP).<sup>[37]</sup> The Projector Augmented Wave (PAW) method is applied to describe the electron-ion interactions, while the exchange correlation energy is described by the scheme of Perdew-Burke-Ernzerhof (PBE) in Generalized Gradient Approximation (GGA). Activation barriers are calculated using the Climbing Image-Nudged Elastic Band (CI-NEB) method. The applications of DFT in ion transport mainly include calculation of migration energy barrier, the influence of defects (as shown in Figure 4<sup>[36]</sup>), conduction mechanism, electronic band structure and so on, which will be reported in detail in part 3.2.

### 2.2.2.2. Molecular Dynamics

The transport of atoms and ions in materials at finite-temperature field can be studied by Molecular Dynamics (MD)

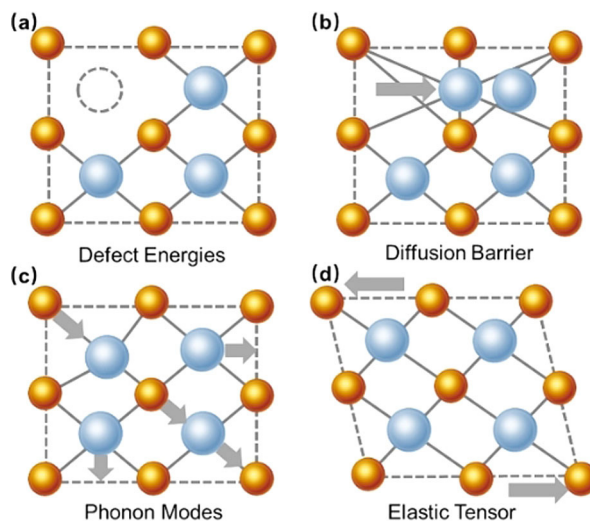


**Figure 4.** Simplified applications of Density Functional Theory.<sup>[36]</sup> Reprinted (adapted) with permission from ref. 36. Copyright (2016) Springer Nature.

simulation. As an atomic-scale simulation method using empirical potential functions, MD can perform larger-scale simulations and can well represent and analyze ion dynamic diffusion processes. The goal is to simulate the evolution of the system over time for a sufficient amount of time to produce enough configuration to meet the phase space we need, and then average these structures to obtain macroscopic properties such as kinetics and thermodynamics.

Figure 5 shows the process of molecular dynamics simulation. The Maxwell-Boltzmann distribution is usually chosen for the velocity distribution. At a certain temperature  $T$ , the distribution function gives the probability  $p$  that the particle has velocity  $v_x$  in the  $x$  direction is as shown in formula (2):

$$p = \left( \frac{m_i}{2\pi k_B T} \right)^{1/2} \exp\left(-\frac{m_i v_{ix}^2}{2k_B T}\right) \quad (2)$$

Knowing the initial position and velocity of the particle, force of each atom can be calculated, and then calculate the displacement  $r(t + \Delta t)$  and velocity  $v(t + \Delta t)$  during the time

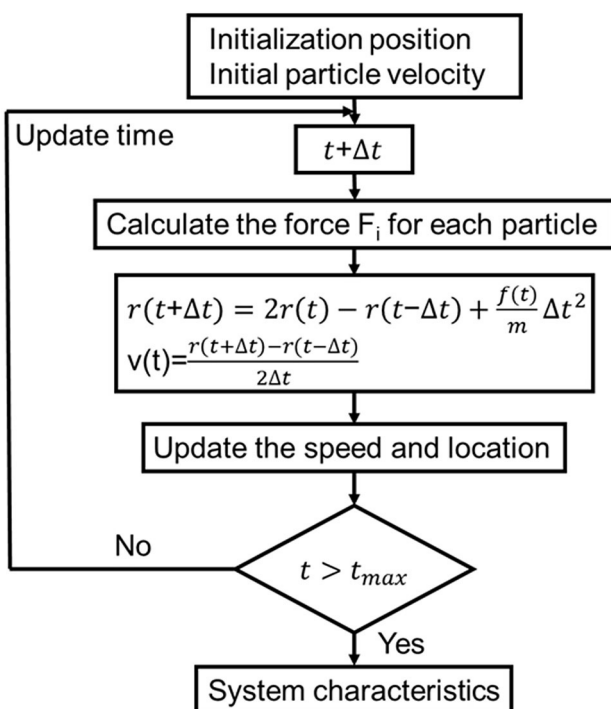


Figure 5. Schematic of molecular dynamics simulation.

$t + \Delta t$  to update the position and velocity of the particle, and repeat the process until the result is obtained. MD can well demonstrate the dynamic diffusion of ions because ions move far enough (multi-nanoseconds) on the time scale achievable by MD to determine transport properties, and the lifetime and solvation structure of ion aggregates are also short enough to allow balanced sampling of the MD time scale. So it is usually used to study transport mechanisms, diffusivity and migration paths in electrolytes.

In addition to the simulation methods mentioned above, the Monte Carlo (MC) method is also commonly used in simulation studies on particle transport. The principle is to simulate a large number of random events that satisfy the physical laws, and then the values of the physical quantities that calculated from these random events are obtained. For example, Van der Ven et al.<sup>[38]</sup> used clustering extensions in dynamic Monte Carlo simulations to describe the configuration dependence of migration barriers, predicting diffusivity that vary by several orders of magnitude with Li concentration, and the results show the diffusivity reaches the maximum when  $x = 0.5$ . In addition to atomic-scale simulations, phase-field methods, molecular mechanics, and finite element analysis are also commonly used to calculate the transport of ions in battery materials. For example, Yamakawa et al.<sup>[39]</sup> simulated the effect of different grain size and grain orientation on the  $\text{Li}^+$  diffusion of layered cathode material  $\text{LiCoO}_2$  by phase field method. Garofalini et al.<sup>[40]</sup> used the molecular force field method to study the mechanism of the conversion reaction of lithium metal in the nanomaterial  $\text{FeF}_2$  in LIB.

### 3. Survey of Recent Research to Improve Ion Conduction

In this section, the recent advances in ion conduction of AMIBs are investigated. The typical ionic diffusivity and conductivity values for different parts of alkaline metal-ion batteries are statistically compared and listed in section 3.1. Computational studies related to ion conduction are reported in section 3.2. In section 3.3, the recent studies including the effects of crystal structure, doping and compounding, as well as novel material synthesis and modification methods are reported.

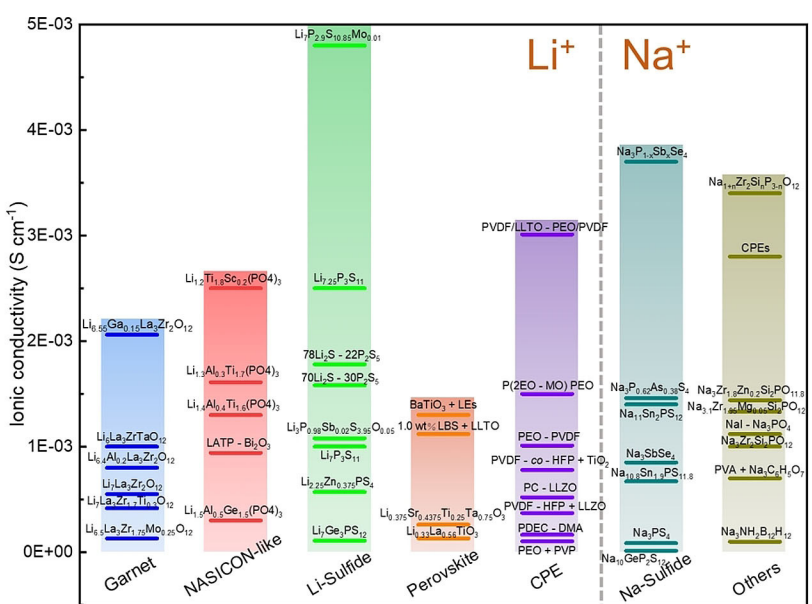
#### 3.1. Recently Reported Ionic Diffusivity and Conductivity

Table 5 shows the ionic diffusivity of the alkali metal ions in different kinds of electrode materials reported in recent years, along with the methods (see 2.2.1 for details) used to calculate it. The use of conductive compounds (such as carbon) as coating materials is an effective means to improve the diffusivity,<sup>[41]</sup> because it can effectively improve the electronic conductivity of the electrode material, thereby affect the diffusion properties of ions. Metal oxides<sup>[41d,9,42]</sup> show potential as electrode materials with excellent ionic diffusivity, and their diffusivity distribution is also very broad ( $10^{-9} \sim 10^{-17} \text{ cm}^2 \text{ s}^{-1}$ ), which strongly depends on their own microstructure (e.g. nanofibers, nanosheets,<sup>[42a,c]</sup> porous spheres,<sup>[41d,42b,d]</sup> or cubic,<sup>[42e]</sup> relevant experimental synthesis methods of which are described in section 3.3.3. For example, Kim et al.<sup>[42f]</sup> prepared shape-controlled  $\text{Cu}_2\text{O}$  nanostructures as anode materials for LIB, exhibiting good diffusivity of  $4.65 \times 10^{-9} \text{ cm}^2 \text{ s}^{-1}$  due to the plane favoring lithium ion transport.  $\text{Li}_{2.97}\text{Mg}_{0.03}\text{VO}_4$  prepared by doping Mg in  $\text{Li}_3\text{VO}_4$  showed surprising diffusivity ( $4.03 \times 10^{-8} \text{ cm}^2 \text{ s}^{-1}$ ).<sup>[43]</sup> Similarly, different levels of B-doped  $\text{TiO}_2$  show a greatly increased diffusion performance (from  $2.5 \times 10^{-12}$  to  $6.06 \times 10^{-11} \text{ cm}^2 \text{ s}^{-1}$ ),<sup>[42b]</sup> and how doping and compounding affect materials performance will be reported in section 3.3.2. In addition, people also focus on phosphates with NASICON-like structure,<sup>[41e,f,44]</sup> but generally, their diffusivity is not very high ( $10^{-13} \sim 10^{-16} \text{ cm}^2 \text{ s}^{-1}$ ), while Prussian blue analogues<sup>[45]</sup> and the ternary material<sup>[46]</sup> exhibited good diffusion properties as cathode materials. Studies on silicon and silicon-carbon anode materials have also revealed their potential to be used as active materials for power batteries.<sup>[47]</sup> Besides, hard carbon synthesized by different methods<sup>[46c,48]</sup> also shows good diffusivity ( $10^{-9} \sim 10^{-10} \text{ cm}^2 \text{ s}^{-1}$ ) for  $\text{Na}^+$  and  $\text{K}^+$  ions.

The investigation of ionic conductivity in solid electrolytes at room temperature reported in the last two years is shown as the histogram in Figure 6 (The highest/lowest ionic conductivity of the various structural families counted here does not represent the limits they can achieve, but only based on the studies reported during this period). We have made a simple classification of the structural family, including Garnet type represented by  $\text{Li}_x\text{La}_3\text{Zr}_2\text{O}_{12}$ ,<sup>[57]</sup> NASICON-like represented by  $\text{Li}_{1+x}\text{Al}_x\text{Ti}_{2-x}(\text{PO}_4)_3$  (LATP),<sup>[58]</sup> Lithium-Sulfide represented by  $\text{Li}_3\text{PS}_4$  (LISICON-like) and  $\text{Li}_2\text{S}-\text{P}_2\text{S}_5$  glass ceramics,<sup>[59]</sup> Perovskite repre-

**Table 5.** Investigation of recently reported diffusivity in electrode materials.

	Ion	Material	Diffusivity [cm <sup>2</sup> S <sup>-1</sup> ]	Method	Year	Ref.
Cathode	Li <sup>+</sup>	LiFePO <sub>4</sub> /C	7.92 × 10 <sup>-12</sup>	EIS	2016	[41a]
		Li <sub>4</sub> Ti <sub>5</sub> O <sub>12</sub> /C	1.00 × 10 <sup>-10</sup>	EIS	2015	[41b]
		Li <sub>4</sub> Ti <sub>5</sub> O <sub>12</sub> -rGO	1.43 × 10 <sup>-11</sup>	CV	2015	[49]
		Nb <sub>2</sub> O <sub>5</sub>	10 <sup>-13</sup> ~ 10 <sup>-12</sup>	GITT + EIS	2013	[42a]
		FeS <sub>2</sub>	1.79 × 10 <sup>-12</sup>	EIS	2016	[50]
		Fe <sub>3</sub> O <sub>4</sub> /C	4.5 × 10 <sup>-13</sup>	EIS	2016	[41d]
		Li <sub>3</sub> VO <sub>4</sub> /C	4.13 × 10 <sup>-11</sup>	CV	2015	[41c]
		Li <sub>2.97</sub> Mg <sub>0.03</sub> VO <sub>4</sub>	4.03 × 10 <sup>-8</sup>	EIS	2016	[43]
		KNi[Fe(CN) <sub>6</sub> ]	10 <sup>-9</sup> ~ 10 <sup>-8</sup>	GITT	2015	[45b]
		CoP	1.29 × 10 <sup>-8</sup>	CV	2017	[51]
		Li(Ni <sub>0.5</sub> Co <sub>0.2</sub> Mn <sub>0.3</sub> )O <sub>2</sub>	1.15 × 10 <sup>-9</sup>	EIS	2016	[46]
		Na <sub>3</sub> V <sub>2</sub> (PO <sub>4</sub> ) <sub>2</sub> F <sub>3</sub>	10 <sup>-12</sup>	EIS	2014	[52]
Anode	Na <sup>+</sup>	Na <sub>3</sub> V <sub>1.95</sub> Mg <sub>0.05</sub> (PO <sub>4</sub> ) <sub>3</sub> /C	1.0 × 10 <sup>-13</sup>	EIS	2015	[41e]
		Na <sub>1.25</sub> V <sub>3</sub> O <sub>8</sub>	1.0 × 10 <sup>-12</sup>	EIS	2015	[53]
		Na <sub>2</sub> MnPO <sub>4</sub> F	4.01 × 10 <sup>-16</sup>	EIS	2017	[44]
		K <sub>x</sub> Mn <sub>1-x</sub> Co <sub>x</sub> Fe(CN) <sub>6</sub>	4.04 × 10 <sup>-11</sup>	EIS	2016	[45a]
		Na <sub>x</sub> CoO <sub>2</sub>	2.2 × 10 <sup>-10</sup>	EIS	2015	[54]
		CuO	3.6 × 10 <sup>-14</sup>	CV	2016	[41f]
		KTi <sub>2</sub> (PO <sub>4</sub> ) <sub>3</sub> /C	2.37 × 10 <sup>-13</sup>	EIS	2016	[55]
		PODG (Graphene)	1.867 × 10 <sup>-10</sup>	EIS	2017	[42b]
		TiO <sub>2</sub>	2.5 × 10 <sup>-12</sup>	CV	2014	
		2 wt% B + TiO <sub>2</sub>	5.4 × 10 <sup>-12</sup>			
		10 wt% B + TiO <sub>2</sub>	6.06 × 10 <sup>-11</sup>			
		Li <sub>4</sub> Ti <sub>5</sub> O <sub>12</sub>	7.434 × 10 <sup>-10</sup>	CV	2016	[41h]
Anode	K <sup>+</sup>	Li <sub>4</sub> Ti <sub>5</sub> O <sub>12</sub> /C	4.293 × 10 <sup>-9</sup>			[42e]
		MnO-C	3.33 × 10 <sup>-13</sup>	EIS	2016	[42d]
		SnO <sub>2</sub> @PPy	1.2 × 10 <sup>-9</sup>	CV	2014	[42f]
		Cu <sub>2</sub> O	4.65 × 10 <sup>-9</sup>	CV	2015	[47a]
		Si	10 <sup>-13</sup> ~ 10 <sup>-12</sup>	GITT	2015	[47b]
		SiO <sub>0.95</sub> C <sub>3.72</sub>	10 <sup>-9</sup> ~ 10 <sup>-10</sup>	PITT, EIS	2014	[56]
		Ge/CNs	10 <sup>-10</sup> ~ 10 <sup>-11</sup>	GITT	2016	[56]
		Hard carbon microspheres (HCS)	2.23 ~ 5.96 × 10 <sup>-12</sup>	EIS	2016	[6c]
		sucrose-based hard carbon(SHC)	Insertion: 6 × 10 <sup>-10</sup> ~ 1.7 × 10 <sup>-9</sup> Extraction: 1.04 × 10 <sup>-9</sup> ~ 1.46 × 10 <sup>-9</sup>	GITT	2016	[6c]
		SnO <sub>2</sub>	0.48 ~ 4.7 × 10 <sup>-10</sup>	PITT	2015	[48]
		SnO <sub>2</sub> /C	1.85 × 10 <sup>-17</sup>	EIS	2016	[41g]
K <sup>+</sup>	Hard carbon microspheres (HCS)	Bi <sub>2</sub> O <sub>3</sub>	7.95 × 10 <sup>-16</sup>			[42g]
		Insertion: 4.8 × 10 <sup>-10</sup> ~ 1.3 × 10 <sup>-9</sup> Extraction: 8.8 × 10 <sup>-10</sup> ~ 1.22 × 10 <sup>-9</sup>	EIS	2015	[6c]	
			GITT	2016	[6c]	



**Figure 6.** Investigation of recently (2017–2018) reported ionic conductivity in solid-state electrolytes at room temperature, including Garnet,<sup>[57]</sup> NASICON-like,<sup>[58]</sup> Li-Sulfide,<sup>[59]</sup> Perovskite,<sup>[60]</sup> Composite polymer electrolyte CPE,<sup>[61]</sup> Na-Sulfide,<sup>[59,62]</sup> Others.<sup>[61c,63]</sup>

sented by  $\text{Li}_{3-x}\text{La}_{2/3-x}\square_{1/3-x}\text{TiO}_3$  (LLTO),<sup>[60]</sup> and various composite polymer electrolytes (CPEs).<sup>[61]</sup> For the  $\text{Na}^+$  solid-state electrolytes, the ionic conductivity of sodium sulfide<sup>[59,62]</sup> and various structures (NASICON type, borohydride, etc.)<sup>[61c,63]</sup> are mainly counted. The  $\text{K}^+$  solid-state electrolytes are no longer listed here due to the lack of reports. In the Garnet type structure, the ionic conductivity can be largely regulated by cation doping, the highly self-textured garnet-type lithium-ion conducting solid electrolyte of LLZO–Ga exhibits an extremely high ionic conductivity ( $2.06 \times 10^{-3} \text{ S cm}^{-1}$  at room temperature).<sup>[57c]</sup> Similarly, in NASICON-like structure,  $\text{Li}_{1+x}\text{Ti}_{2-x}\text{Sc}_x(\text{PO}_4)_3$  doped with Sc exhibits an ion conductivity of up to  $2.5 \times 10^{-3} \text{ S cm}^{-1}$  ( $X = 0.2$ ).<sup>[58a]</sup> This is comparable to or even better than the LATP<sup>[58d,e]</sup> reported in the literature. In Lithium Sulfides,  $\text{Li}_{10}\text{GeP}_2\text{S}_{12}$  with LISICON-like structure has the highest ionic conductivity reported in this kind of materials (more than  $10^{-2} \text{ S cm}^{-1}$  at room temperature<sup>[59e]</sup>). The ionic conductivity can be improved by adjusting the ratio of the two phases in the  $\text{Li}_2\text{S}-\text{P}_2\text{S}_5$  glass ceramic, the highest ionic conductivity reaches  $4.8 \times 10^{-3} \text{ S cm}^{-1}$  after the doping of  $\text{MoS}_2$ .<sup>[59i]</sup> The ionic conductivity of the Perovskite structure itself is only about  $10^{-4} \text{ S cm}^{-1}$ ,<sup>[60b,d]</sup> but it could be greatly improved after compounding with other materials.<sup>[60a,c]</sup> Studies on solid polymer electrolytes have focused on complexing with metal oxide nanoparticles, LLZO, and various polymers.<sup>[61]</sup> In the study of  $\text{Na}^+$  solid-state electrolytes, the equivalent substitution of  $\text{Na}_3\text{PS}_4$  showed a significant increase in ionic conductivity,<sup>[59i,62a,b]</sup> up to  $3.7 \times 10^{-3} \text{ S cm}^{-1}$ .<sup>[59i]</sup> However, the sodium sulfide  $\text{Na}_{10}\text{GeP}_2\text{S}_{12}$  with similar structure of  $\text{Li}_{10}\text{GeP}_2\text{S}_{12}$  does not show commensurately high ionic conductivity of  $\text{Na}^+$ .<sup>[62e]</sup> The  $\text{Na}_{1+n}\text{Zr}_2\text{SinP}_{3-n}\text{O}_{12}$  possessing a NASICON type structure achieves ionic conductivity of up to  $3.4 \times 10^{-3} \text{ S cm}^{-1}$ , and even reaches  $1.4 \times 10^{-2} \text{ S cm}^{-1}$  at  $80^\circ\text{C}$ . The ionic conductivities of different structural families are strongly dependent on the internal crystal structure and conduction mechanism, which will be discussed in section 3.3.1. The latest computational studies will also be statistically discussed in the following section.

### 3.2. Recently Reported Computational Studies

Density functional theory and molecular dynamics simulation methods are of great significance for studying the internal mechanism of materials and guiding experiments. As shown in Table 6, the recent studies on simulation calculations of ion conduction and diffusion are sorted by different materials and listed in chronological order. They are discussed according to their representative research objects.

The transport of alkali metal ions is an important part of the battery. The path of the transport of alkali metal ions, the energy barrier, etc. are directly related to the rate performance, polarization degree and ionic mutual occupation of the battery. The diffusion properties of ions in the material can be obtained by the Nudged Elastic Band (NEB) method based on the transition state theory, or calculated by a molecular dynamics method based on the first principle. The calculation of ion transport by these methods is the focus of recent re-

search.<sup>[72,80–82,87]</sup> For example, Cakir et al.<sup>[65]</sup> systematically studied the adsorption and diffusion of Li, Na, K and Ca atoms on the  $\text{Mo}_2\text{C}$  monolayer by the first principle method. The predicted migration energy barrier is 43 meV for Li, 19 meV for Na and 15 meV for K, respectively, and this results in the rapid diffusion of these atoms on  $\text{Mo}_2\text{C}$ , while the calculated average voltage of the adsorbed atoms is 0.68 V for Li and 0.30 V for Na, which is suitable for low charging voltage applications. Watcharatharapong et al.<sup>[75]</sup> performed DFT+U calculations to reveal the  $\text{Na}^+$  diffusion mechanism in Kröhnkite-type  $\text{Na}_2\text{Fe}(\text{SO}_4)_2 \cdot 2\text{H}_2\text{O}$  materials. Figure 7 shows the favorable pathway for the

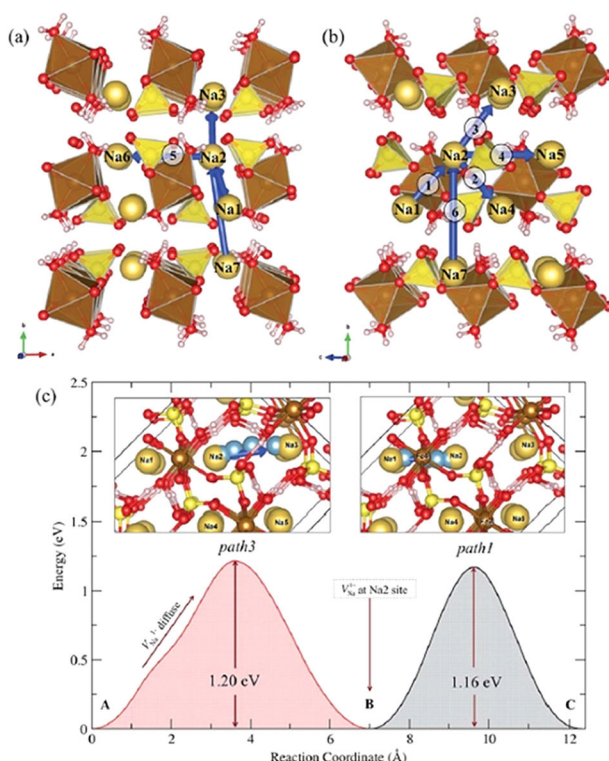


**Figure 7.** Illustration of  $\text{Na}^+$  diffusion pathways in a supercell lattice: (a) in c-axis and (b) in a-axis. (c) Migration barriers of  $V_{\text{Na}}^+$  along MEPs of path 3 and path 1. The insets show the migration pathway of  $\text{Na}^+$  ion in the  $[01\bar{1}]$  direction.<sup>[75]</sup> Reprinted (adapted) with permission from ref. 75. Copyright (2017) Royal Society of Chemistry.

diffusion of  $\text{Na}^+$  in  $\text{Na}_2\text{Fe}(\text{SO}_4)_2 \cdot 2\text{H}_2\text{O}$ , the calculation of the NEB indicates that the most likely route is still paths 1 and 3 due to structural deformation during migration. The  $\text{Na}^+$  diffusion mainly occurs in the  $[01\bar{1}]$  direction, indicating the possibility of defect-assisted diffusion. Noda et al.<sup>[84]</sup> calculated the electrochemical window of  $\text{LiZr}_2(\text{PO}_4)_3$  (LZP) and the transport of lithium ions. The calculated Li-ion conductivity at room temperature ( $5.0 \times 10^{-6} \text{ S cm}^{-1}$ ) and the activation energy (0.43 eV) for Li-ion diffusion are in fair agreement with experimental results. It is found that each Li ion migrates between 6b sites as it is pushed out or repelled by other Li ions around these 6b sites by analyzing the Li-ion trajectories in the FPMD simulations. Hence, the high Li-ion conductivity is attributed to a migration mechanism driven by Frenkel-like defect. Dive et al.<sup>[90]</sup> em-

**Table 6.** Recent researches on simulation calculations of alkali ion conduction.

Material	Description of the research object	Method	Year	Reference
Anode	Phosphorene	DFT	2015	[64]
	Mo <sub>2</sub> C	DFT	2016	[65]
	MoO <sub>2</sub>	DFT + MD	2017	[66]
	2D layered PFs	DFT	2017	[67]
	TCNB	DFT	2017	[68]
	NbSe <sub>2</sub>	DFT	2017	[69]
Cathode	Na <sub>3</sub> V <sub>2</sub> (PO <sub>4</sub> ) <sub>3</sub> (NVP)	DFT	2014	[70]
	LiMnO <sub>2</sub> and Li <sub>2</sub> MnO <sub>3</sub>	DFT	2015	[71]
	Na <sub>2+</sub> δFe <sub>2</sub> δ <sub>1/2</sub> (SO <sub>4</sub> ) <sub>3</sub>	DFT + MD	2015	[72]
	δ-NH <sub>4</sub> V <sub>4</sub> O <sub>10</sub>	DFT	2016	[73]
	FePO <sub>4</sub> /LiFePO <sub>4</sub>	DFT	2016	[74]
	Na <sub>2</sub> Fe(SO <sub>4</sub> ) <sub>2</sub> ·2H <sub>2</sub> O	DFT + U	2017	[75]
	Na <sub>x</sub> Co <sub>1-y</sub> Mn <sub>y</sub> O <sub>2</sub>	DFT	2017	[76]
	Na <sub>3</sub> V <sub>2-x</sub> Al <sub>x</sub> (PO <sub>4</sub> ) <sub>3</sub>	DFT	2018	[77]
	Li <sub>10</sub> GeP <sub>2</sub> S <sub>12</sub> (LGPS)	MD	2012	[78]
	Li <sub>7</sub> La <sub>3</sub> Zr <sub>2</sub> O <sub>12</sub> (LLZO)	DFT + MD	2014	[79]
Electrolyte	LiAlPO <sub>4</sub> F and LiMgSO <sub>4</sub> F	DFT	2014	[80]
	LiTi <sub>2</sub> (PO <sub>4</sub> ) <sub>3</sub> (LTP)	DFT	2015	[81]
	Li <sub>4</sub> SiO <sub>4</sub> – Li <sub>3</sub> PO <sub>4</sub>	MD	2015	[82]
	Na <sub>3</sub> PSe <sub>4</sub>	DFT + MD	2016	[83]
	LiZr <sub>2</sub> (PO <sub>4</sub> ) <sub>3</sub> (LZP)	DFT + MD	2017	[84]
	LiAlSO	DFT + MD	2017	[85]
	NMP	DFT + MP2	2017	[86]
	LiCF <sub>3</sub> SO <sub>3</sub>	DFT + MD	2017	[87]
	LiAlSiO <sub>4</sub>	MD	2017	[88]
	Na <sub>2</sub> S + SiS <sub>2</sub>	MD	2018	[89]
	Na <sub>3</sub> OCl	DFT	2018	[90]
	small phosphonium-based ILs + LiFSI	MD	2018	[91]
DMF + LiCl	The effect of cation structure on local structuring and ion diffusional and rotational dynamics	MD	2018	[92]
	A number of qualitative properties	MD	2018	[93]
Li <sub>7</sub> La <sub>3</sub> Zr <sub>2</sub> O <sub>12</sub> -LiCoO <sub>2</sub>	The electronic and atomic structure, etc.	DFT	2018	[94]

ployed *ab initio* MD to determine ion conduction mechanisms, to calculate energy barriers for ion hops, and to correlate these to the local short-range structure of 0.50Na<sub>2</sub>S + 0.50SiS<sub>2</sub> glass. The calculated ionic conductivities at room temperature are in the range of  $\sim 10^{-5}$  S cm<sup>-1</sup> for the x=0.50 composition and increased significantly with sodium sulfide (x) content.

In addition to the study of diffusion paths and energy barriers, it is also critical to simulate the effects of defects and vacancies in battery materials.<sup>[71,83,95]</sup> Guo et al.<sup>[64]</sup> systematically investigated the pristine and defect-containing phosphorene as anode materials for Li-ion batteries (LIBs) by first-principles calculations. The results suggest that the binding energies of Li adsorption on the different sites vary within a narrow range, that the binding between Li atom and pristine phosphorene is relatively weak, and that the defect can greatly improve the performance of the phosphorene. The diffusion path and barrier of Li atom on SVP are shown in Figure 8, The binding energy of Li around the vacancy is increased about 1 eV compared to that of the perfect phosphorene. More importantly, Li atoms could diffuse between two adjacent grooves with an energy barrier of 0.13 eV, which opens a novel channel

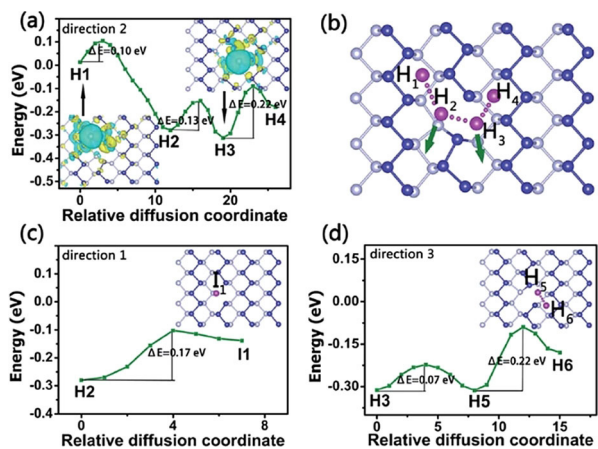


**Figure 8.** (a) The diffusion barrier of Li atom on SVP (direction 2) and the charge density difference for Li adsorption on H1 and H3 sites. Yellow surfaces correspond to charge gains and the blue surfaces correspond to an equivalent charge lost. (b) The adsorption sites (H1, H2, H3, and H4) and diffusion path of Li atom on SVP. (c) The adsorption site (I1) and diffusion barrier (direction 1). (d) The adsorption sites (H5, H6) and diffusion barrier (direction 3).<sup>[64]</sup> Reprinted (adapted) with permission from ref. 64. Copyright (2015) Royal Society of Chemistry.

for Li diffusion. Wan et al.<sup>[91]</sup> carried out *ab initio* calculations to study various properties of  $\text{Na}_3\text{OCl}$ , namely the formation energies of various neutral defect pairs, the defect hopping barriers, the solution energies of high valence alkali earth metal substituted to the Na atoms, and the effect of such substitution to the Na migration. The result suggests that, in the pristine  $\text{Na}_3\text{OCl}$  antiperovskite, the formation of NaCl Schottky defect pairs is energetically more favorable than the other defect pairs studied. Consequently, it is likely that Na transport is enabled by a vacancy hopping mechanism, in analogy with  $\text{Li}_3\text{OCl}$ .

The resistance at the grain boundary (GB), which is even higher than of the ions inside the lattice, greatly affects the conduction of ions. Changes of charge-carrier concentration are often occurring at these interfaces, and these effects are generally detrimental to ionic conductivity. Although many reports have pointed out this phenomenon,<sup>[96]</sup> they are rarely quantified or described on an atomic scale. Recent research by Dawson et al.<sup>[97]</sup> further reinforced the basic understanding in this aspect. The possible conduction mechanism of Li ions between the unit cell and the grain boundary is shown in Figure 9a. They construct the symmetric tilted grain boundaries of four different configurations ( $\Sigma 3(111)$ ,  $\Sigma 3(112)$ ,  $\Sigma 5(210)$ , and  $\Sigma 5(310)$ ) using the coincidence grid theory (two separate dies are rotated at a given tilt angle until their surface planes coincide), and calculate their respective grain boundaries energy (Figure 9b, c). The significantly lower GB energy of  $\Sigma 3(111)$  indicates the presence of a high concentration of GB in  $\text{Li}_3\text{OCl}$ . The effect of GB resistance on ionic conductivity was simulated by large-scale molecular dynamics (Figure 9d), the results show that the calculated volume ionic conductivity is  $6.55 \times 10^{-3} \text{ S cm}^{-1}$  at 500 K, which is consistent with the

experimental results. The thermodynamically most stable GB exhibits Li ionic conductivity (about  $10^{-4} \text{ Scm}^{-1}$  at 500 K) that is about one order of magnitude lower than the volume ionic conductivity, which indicating GB resistance. Compared with bulk phase (0.29 eV), all lithium ion mobility activation energy (0.40–0.56 eV) of GB in three directions of X/Y/Z have increased. In addition, the size effect of the grain boundary resistance is also found. When the grain size is less than 100 nm, the total ionic conductivity is controlled by GB. As the grain size increases, the total conductivity increases (Figure 9e). This work reveals the effects of grain boundaries at the atomic level and provides an indication of further understanding of the interface issues involved in other materials.

Another hotspot of computational studies is the structural stability (or phase transition) of the material. Instability of the battery material will lead to rapid decrease of battery performance. The prediction of electrode material stability is mainly based on the calculation of its thermodynamic properties. Zhou Y et al.<sup>[66]</sup> adopted an *ab initio* molecular dynamics simulation and density functional theory calculation to study the stability and electrochemical properties of a  $\text{MoO}_2$  sheet. Identified by a phonon dispersion curve and potential energy curve calculations, the  $\text{MoO}_2$  sheet is proved to be dynamically and thermally stable. Wang et al.<sup>[85]</sup> identified a new layered oxy-sulfide  $\text{LiAlSO}$  of orthorhombic structure as a novel lithium superionic conductor through first-principles calculations and crystal structure prediction techniques. Furthermore, phonon and molecular dynamics simulations verify their dynamic stabilities. Singh et al.<sup>[89]</sup> performed *ab initio* molecular dynamics simulations of  $\beta$ -eucryptite to study the origin of high temperature superionic phase transition in this material. The Li

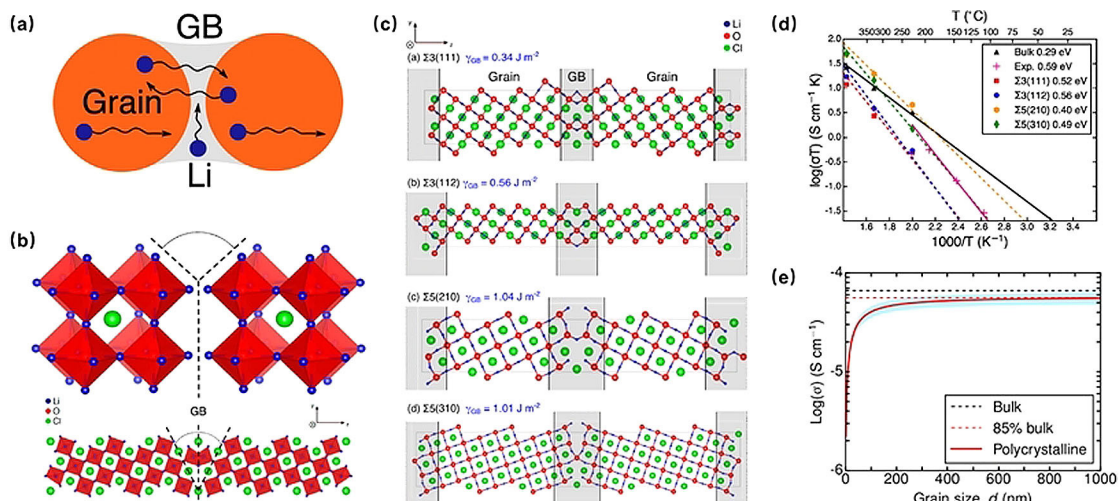


**Figure 9.** (a) Schematic showing possible Li-ion (blue) transport mechanisms at the GB (gray) and grain (orange) of a solid electrolyte material. (b) Schematic of the GB construction process using the cubic anti-perovskite  $\text{Li}_3\text{OCl}$  structure, in which Li, O, and Cl ions occupy the X, B, and A sites of the  $\text{ABX}_3$  perovskite structure. (c) Structures and energies of the (a)  $\Sigma 3(111)$ , (b)  $\Sigma 3(112)$ , (c)  $\Sigma 5(210)$ , and  $\Sigma 5(310)$  GBs. Equivalent GBs are located at the center and edges of each supercell. The x and y directions represent the planes of the GBs, while the z direction is perpendicular to the GB plane. (d)  $\text{Li}^+$  temperature-dependent conductivities ( $\sigma_T$ ) and activation energies ( $E_a$ ) for bulk  $\text{Li}_3\text{OCl}$  and the four GBs. Electrochemical impedance spectroscopy results are included for comparison (e) Evolution of the total conductivity (bulk + polycrystalline) as a function of grain size,  $d$  (in nm), for  $\text{Li}_3\text{OCl}$  at 300 K. The black dashed line is the calculated bulk conductivity. The red curve is the total conductivity of the polycrystalline material, with the blue band representing its upper and lower limits based on different densification behaviors (see SI for details). The red dashed line is the maximum average polycrystalline conductivity, equivalent to 85% of the bulk conductivity.<sup>[97]</sup> Reprinted (adapted) with permission from ref. 97. Copyright (2018) American Chemical Society.

ionic conductivity is found to increase due to the anisotropic negative thermal expansion along the hexagonal c-axis. In addition, the problems focused on computational studies include: electronic structure calculation,<sup>[68–69,94]</sup> ion extraction number studied by discussing ion occupancy,<sup>[70]</sup> ion interaction in ionic liquid (ILs),<sup>[86]</sup> etc.

### 3.3. Recently Reported Strategies to Improve Ion Conduction

#### 3.3.1. Utilizing Crystalline Materials with High Ion Conduction

Diffusion of an alkali metal ion in the crystalline material is strongly dependent upon the interaction potential between the alkali metal ions and the host material structure. Figure 10 shows a lot of representative crystal structures.<sup>[98]</sup> According to the diffusion path of ions in the crystal, various structure types can be classified, such as materials with 1D channel (e.g. LiFePO<sub>4</sub>, Figure 10a), 2D layer structure (e.g. LiCoO<sub>2</sub> and graphite, Figure 10b,e), and 3D diffusion channel (e.g. LiMn<sub>2</sub>O<sub>4</sub>, Figure 10c). However, such classification is not entirely applicable. The research on polymorphic LiFeSO<sub>4</sub>F (tavorite and triplite)<sup>[99]</sup> shows that, although the calculated migration energy proves that both isomorphs are Li<sup>+</sup> conductors, the Li<sup>+</sup> in triplite type LiFeSO<sub>4</sub>F move in a restricted migration path (one or two dimensions), while the tavorite type has continuous three-dimensional conductive network for Li<sup>+</sup>. Similarly, Li<sub>10</sub>GeP<sub>2</sub>S<sub>12</sub> can be classified into a 3D conductor or a pseudo 1D conductor.

The conduction path and mechanism of ions in inorganic solid-state electrolytes (Figure 10f-j) is more complicated. The Garnet type (Figure 10f) is derived from the ideal garnet structure with the general formula A<sub>3</sub>B<sub>2</sub>(XO<sub>4</sub>)<sub>3</sub>, Li<sup>+</sup> ions usually occupy the tetrahedral positions of X-site which is 4-fold coordinated. Meier et al.<sup>[79]</sup> identified the mechanisms (Fig-

ure 11a) responsible for the considerable difference in ionic conductivity between the tetragonal and the cubic phases of LLZO (Li<sub>7</sub>La<sub>3</sub>Zr<sub>2</sub>O<sub>12</sub>). In tetragonal LLZO, the motion of Li ions is of fully collective nature or synchronous, which requires a higher activation energy. However, in cubic LLZO, the asynchronous collective motion of Li ions caused by single ion hopping results in lower activation energy due to the presence of unoccupied Li sites. Substitution of Zr<sup>[100]</sup> with Ta, Sb, etc. can improve the distribution of Li ions in the crystal structure of LLZO and improve the ionic conductivity. Recent reports<sup>[101]</sup> indicate that when stabilizing the garnet-structured LLZO with Ga<sup>3+</sup>, it shows superior properties compared to LLZO stabilized with supervalent cations (such as Al<sup>3+</sup>). In the NASICON-like LiTi<sub>2</sub>(PO<sub>4</sub>)<sub>3</sub> (Figure 10g) framework, Li ions occupy two sites of M1 and M2 (Figure 11b),<sup>[102]</sup> and lithium migration occurs through the jump between these two sites (Figure 11c). The partial occupancy of Li<sup>+</sup> ions at these two sites is critical for fast Li<sup>+</sup> ion conduction. The Li<sup>+</sup> ion conduction activation energy decreases linearly with the bottleneck size between the M1 and M2 sites.<sup>[103]</sup> Li ions are introduced for charge compensation by substitution of a trivalent cation such as Al<sup>3+</sup>, but these additional Li ions are trapped near the trivalent ions, resulting in a limited increase in ion conductivity. The LISICON-like Li<sub>10</sub>GeP<sub>2</sub>S<sub>12</sub> (LGPS) (Figure 10h) has the highest Li<sup>+</sup> ion conductivity<sup>[104]</sup> reported so far because it forms a one-dimensional channel with very high Li mobility. The conduction path of Li<sup>+</sup> ions in the *b* direction and the *c* direction is shown in Figure 11d,<sup>[105]</sup> and the recent theoretical calculation<sup>[106]</sup> shows that it is also possible for Li<sup>+</sup> to diffuse in the *ab* plane. In the latest study, Paulus et al.<sup>[105]</sup> used spin-aligned echo (SAE) nuclear magnetic resonance (NMR) techniques to directly detect the slow Li<sup>+</sup> ion transitions with correlation times as low as about 10<sup>-5</sup> s, which provides a new way to understand the mobility of Li<sup>+</sup> in three dimensions. By introducing Li ions into the perovskite structure by heterovalent ion doping, a

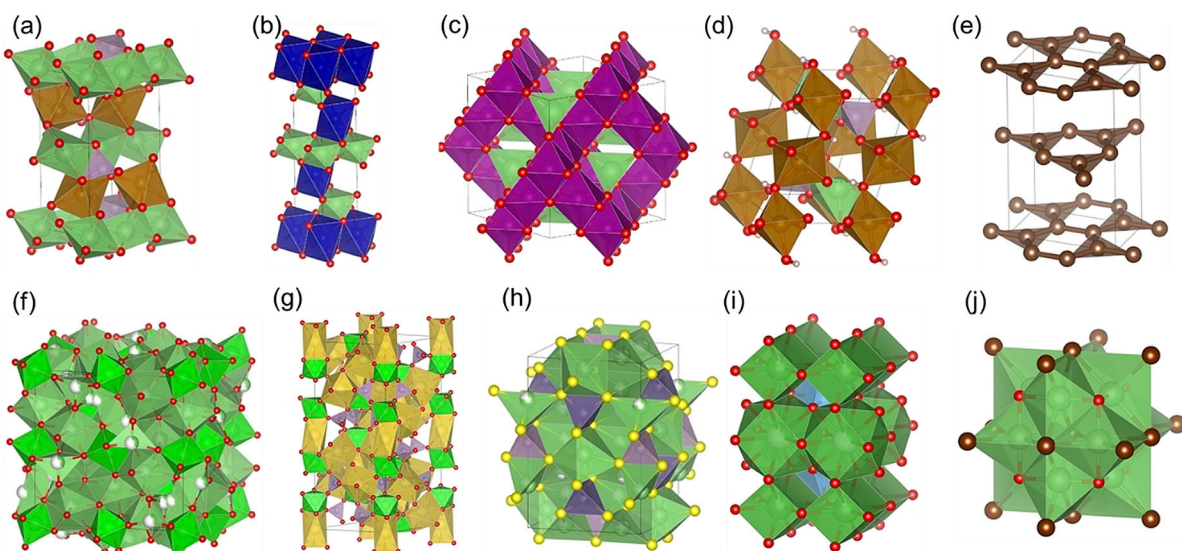


**Figure 10.** Some typical crystal structures of battery materials: (a) Olivine LiFePO<sub>4</sub>, (b) Layered LiCoO<sub>2</sub>, (c) Spinel LiMn<sub>2</sub>O<sub>4</sub>, (d) Tavorite LiFeSO<sub>4</sub>F, (e) Graphite, (f) Garnet Li<sub>2</sub>La<sub>3</sub>Zr<sub>2</sub>O<sub>12</sub>, (g) NASICON-like Na<sub>3</sub>Zr<sub>2</sub>Si<sub>2</sub>PO<sub>12</sub>, (h) LISICON-like Li<sub>10</sub>GeP<sub>2</sub>S<sub>12</sub>, (i) Perovskite Li<sub>3x</sub>La<sub>2/3-x</sub>□<sub>1/3-x</sub>TiO<sub>3</sub> and(j) Antiperovskite Li<sub>3</sub>OCl.<sup>[98]</sup>

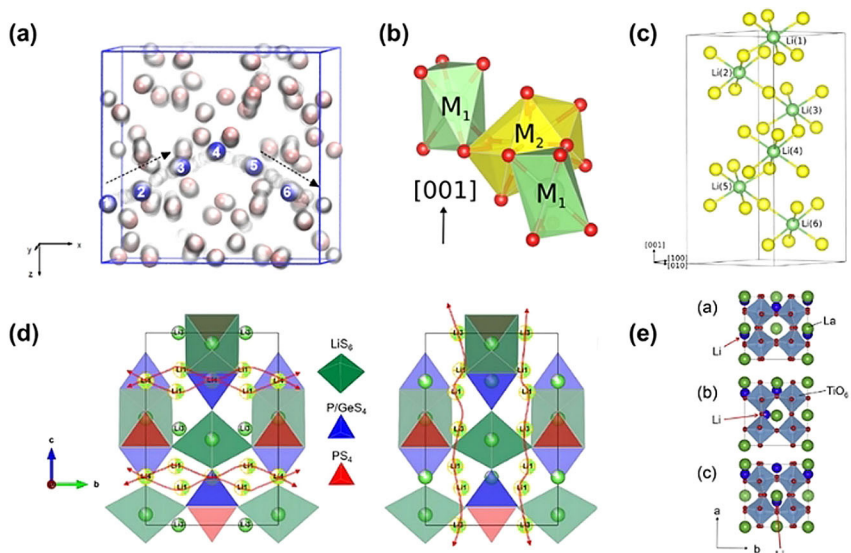


**Figure 11.** Migration pathway of lithium ions in different kinds of solid-state electrolytes: (a) Li-ion positions of tetragonal LLZO as observed from metadynamics simulation at 300 K. Transparent gray: all Li-ion positions visited during 10 ps run. Solid: starting configuration of Li ions. Blue: ions involved in collective motion. Arrows indicate the direction of motion.<sup>[79]</sup> Reprinted (adapted) with permission from ref. 79. Copyright (2014) American Chemical Society. (b)&(c) M1 and M2 sites of Li atoms in the crystal structure of oLiTi<sub>2</sub>(PO<sub>4</sub>)<sub>3</sub> & Migration path for Li ion in oLiTi<sub>2</sub>(PO<sub>4</sub>)<sub>3</sub> consisting of M1(stable sites in green) and M2 (transition sites in yellow) positions.<sup>[102]</sup> Reprinted (adapted) with permission from ref. 102. Copyright (2015) American Chemical Society. (d) Structure of LGPS and coordination polyhedron GeS<sub>4</sub>, PS<sub>4</sub> and LiS<sub>6</sub>. Red arrows illustrate the Lithium pathways in the ab plane (left structure) and in the channels along the c direction (right structure).<sup>[105]</sup> Reprinted (adapted) with permission from ref. 105. Copyright (2018) Elsevier. (e) Calculated structures during Li migration in bulk LLTO corresponding to starting-point, end-point and middle-point positions. Migrating Li ions are indicated by red arrows.<sup>[108]</sup> Reprinted (adapted) with permission from ref. 108. Copyright (2015) Elsevier.

composition of  $\text{Li}_{3x}\text{La}_{2/3-x}\square_{1/3-x}\text{TiO}_3$  (Figure 10i) can be obtained. The introduction of  $\text{Li}^+$  ions changes the concentration of lithium and vacancies, and its interaction<sup>[107]</sup> can significantly affect ionic conductivity. LLTO has a high volume ionic conductivity, but due to the high electrical resistance at the grain boundaries, its total conductivity tends to be two orders of magnitude lower than the volume ion conductivity.

Figure 11e shows the migration of lithium ions in LLTO, the calculations by Moriwake et al.<sup>[108]</sup> show that the Li ions migration barrier at the 90° domain boundary that completely occupies La ions can be as high as 3.58 eV from the NEB calculation. If Li ions migrate through the La ions vacancy at the domain boundary, the barrier is reduced to 0.58 eV, and if Li ions penetrates the domain boundary through the La-poor (Li rich) layer, it can be further reduced to 0.26 eV, which is almost the same as the barrier energy found in bulk LLTO. The new series of lithium-rich materials antiperovskite  $\text{Li}_3\text{OX}$  ( $X = \text{Cl}$  or  $\text{Br}$ ) (Figure 10j) have received increasing attention lately,<sup>[109]</sup> and first principles studies have shown high ionic conductivity ( $> 10^{-3} \text{ S cm}^{-1}$  at room temperature) and low migration barriers for Li ion transport (0.2–0.3 eV). Other solid-state electrolytes such as Li-Nitride, Li-Hydride, and Li-Halide are no longer listed here due to the much lower ionic conductivity compared with those mentioned above. In addition, New insights<sup>[110]</sup> on crystal structure have also been reported, e.g. the synthesis of polycrystalline  $\text{Li}_2\text{SnS}_3$  by high temperature solid phase method and simulated its structure and conduction mechanism. The  $\text{Li}^+$  ion conductivity at 100 °C is as high as  $1.6 \times 10^{-3} \text{ S cm}^{-1}$ , which is the highest among the ternary chalcogenides. Bo et al.<sup>[111]</sup> studied the isomorphic cubic  $\text{Na}_3\text{PS}_4$  and  $\text{Na}_3\text{PSe}_4$  as fast  $\text{Na}^+$

conductors, indicating that the formation of defects in the structure may be the key factor leading to high ionic conductivity. Zhang et al.<sup>[112]</sup> reported a new sodium superionic conductor  $\text{Na}_{11}\text{Sn}_2\text{PS}_{12}$ , which is crystallized in an unprecedented three-dimensional structure, exhibiting an ionic conductivity of  $1.4 \text{ mS cm}^{-1}$  and a very low activation energy barrier of 0.25 eV for Na ion migration. Chen et al.<sup>[113]</sup> incorporate cationic skeleton into the COF structure to split the Li salt ions pair through stronger dielectric screening. It is observed that the concentration of free Li ions in the resulting material is drastically increased, leading to a significantly improved  $\text{Li}^+$  conductivity in the absence of any solvent (up to  $2.09 \times 10^{-4} \text{ S cm}^{-1}$  at 70 °C).

By utilizing crystalline materials with high ion conduction, high performance batteries can be constructed.<sup>[114]</sup> Recently, Liu et al<sup>[115]</sup> reported a strategy to build high-voltage K–Na hybrid aqueous battery, which based on  $\text{K}_2\text{FeFe}(\text{CN})_6$  cathode and carbon coated  $\text{NaTi}_2(\text{PO}_4)_3$  (NTP/C) anode. Due to the unique cation selectivity of both materials and ultrafast ion conduction of NTP/C, the hybrid battery delivers a high capacity of  $160 \text{ mAh g}^{-1}$  at a 0.5 C rate. As shown in Figure 12. The fast ion conduction (the  $\text{K}^+$  diffusion coefficient of K-FeHCF is ca.  $1.7 \times 10^{-13} \text{ cm}^2 \text{s}^{-1}$ , and the  $\text{Na}^+$  diffusion coefficient of NTP/C is ca.  $3.0 \times 10^{-11} \text{ cm}^2 \text{s}^{-1}$ ) and selective cation channels (which is priority selection towards  $\text{K}^+$  of K-FeHCF and single- $\text{Na}^+$  selectivity of NTP/C) of both cathode and anode materials ensure ultrahigh performances of the fabricated HAB.

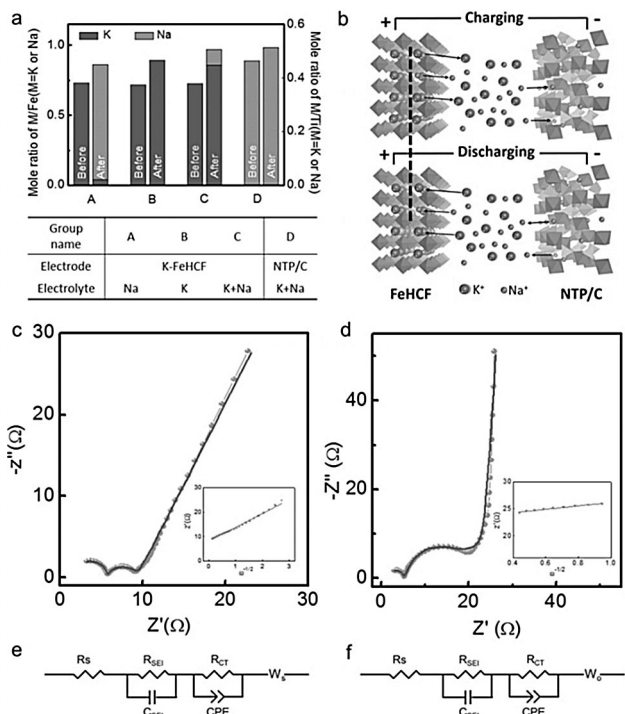


**Figure 12.** (a) Element content of the K-FeHCF and NTP/C electrodes before and after 100 charge/discharge cycles at 1 C rate, respectively. (b) Schematic of the K-Na HAB. EIS curves within the frequency range from 100 kHz to 10 mHz of the K-FeHCF in electrolyte K (c) and NTP/C in electrolyte Na (d), respectively. The insets are corresponding linear fitting curves. (e,f) Equivalent electric circuits of the above EIS patterns.<sup>[115]</sup> Reprinted (adapted) with permission from ref. 115. Copyright (2018) John Wiley & Sons.

### 3.3.2. Doping and Compounding

Element substitution by doping is an important means to improve transmission dynamics of ions in alkali metal ion batteries. For example, the ionic conductivity of  $\text{Li}_{2.97}\text{Mg}_{0.03}\text{VO}_4$  prepared by adding Mg to  $\text{Li}_3\text{VO}_4$  is increased by two orders of magnitude (from  $1.66 \times 10^{-10} \text{ Scm}^{-1}$  for the pure  $\text{Li}_3\text{VO}_4$  to  $4.37 \times 10^{-8} \text{ Scm}^{-1}$  for the  $\text{Li}_{2.97}\text{Mg}_{0.03}\text{VO}_4$ ), and the ionic diffusivity is also increased from  $1.24 \times 10^{-8} \text{ cm}^2 \text{s}^{-1}$  to  $4.03 \times 10^{-8} \text{ cm}^2 \text{s}^{-1}$ .<sup>[43]</sup> The  $\text{TiO}_2$  doped with different contents of B also show a greatly increased diffusion performance ( $2.5 \times 10^{-12} \sim 6.06 \times 10^{-11} \text{ cm}^2 \text{s}^{-1}$ ).<sup>[42b]</sup> Generally, there is a critical value for the substitution concentration, above which, the distortion of the lattice is so strong that the increase in the migration energy or the decrease in extrinsic defects surpasses the effect of increasing the concentration of mobile species. For instance, Figure 13<sup>[41e]</sup> shows the kinetic properties of  $\text{Na}_3\text{V}_{2-x}\text{Mg}_x(\text{PO}_4)_3/\text{C}$  compounds with different  $\text{Mg}^{2+}$  doping contents ( $x = 0, 0.01, 0.03, 0.05, 0.07$  and  $0.1$ ) prepared by a simple sol-gel method. The results show that the electronic conductivity increases with the increase of the doping content, while the diffusivity shows a critical value at  $x = 0.05$ , and when  $x > 0.05$ , it begins to show a downward trend. Jiang et al.<sup>[45a]</sup> also studied the electrochemical properties of different content of Co substituted  $\text{K}_2\text{Mn}_{1-x}\text{Co}_x\text{Fe}(\text{CN})_6$  with different content of Co substitution. The

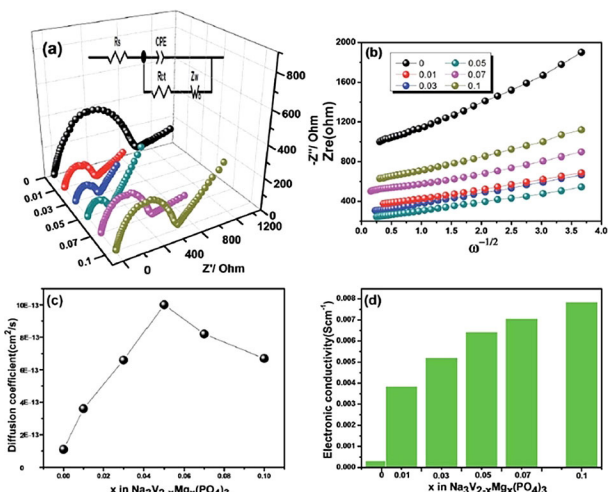


**Figure 13.** (a) Nyquist plots of the  $\text{Na}_3\text{V}_{2-x}\text{Mg}_x(\text{PO}_4)_3$  ( $x = 0, 0.01, 0.03, 0.05, 0.07$  and  $0.1$ ); inset: the equivalent circuit used to fit the EIS. (b) The relationship between  $Z_{re}$  and  $\omega^{-1/2}$  at low frequencies. (c) Sodium ion diffusion coefficients in  $\text{Na}_3\text{V}_{2-x}\text{Mg}_x(\text{PO}_4)_3/\text{C}$  ( $x = 0, 0.01, 0.03, 0.05, 0.07$ , and  $0.1$ ). (d) Electronic conductivity of  $\text{Na}_3\text{V}_{2-x}\text{Mg}_x(\text{PO}_4)_3/\text{C}$  ( $x = 0, 0.01, 0.03, 0.05, 0.07$ , and  $0.1$ ), which was taken using a RTS-4 linear four-point probe measurement system.<sup>[41e]</sup> Reprinted (adapted) with permission from ref. 41e. Copyright (2015) Royal Society of Chemistry.

results show that when  $X=0.1$ , it has the highest diffusion coefficient of  $4.04 \times 10^{-11} \text{ cm}^2 \text{s}^{-1}$ .

Since different ions have different ionic radii, the introduction of other elements usually produces a change in lattice parameters<sup>[116]</sup> or phase transitions.<sup>[101]</sup> Figure 14a<sup>[117]</sup> shows the doping concentration dependence of the unit cell volume of  $\text{Li}_3\text{K}_3\text{Ce}_2(\text{BH}_4)_{12}$  and  $\text{Li}_3\text{K}_3\text{La}_2(\text{BH}_4)_{12}$  for different divalent cation ( $\text{Ca}^{2+}, \text{Sr}^{2+}, \text{Eu}^{2+}$ ) substitutions. For  $\text{Sr}^{2+}, \text{Eu}^{2+}$  cations, the unit cell volume increases significantly as the doping concentration increases, and as a result, the  $\text{Li}^+$  ionic conductivities of the samples doped with divalent  $\text{Sr}^{2+}$  and  $\text{Eu}^{2+}$  are increased by an order of magnitude (Figure 14b/c) over the entire temperature range. So how does the change in lattice volume caused by doping of different elements affect the ionic conductivity? The key is that the increase in lattice volume can effectively reduce the activation energy within a certain range. Bachman et al.<sup>[25]</sup> made detailed statistics on change of activation energy and ionic conductivity changes caused by lattice volume. The study by Lang et al.<sup>[102]</sup> also proves that the substitution of Ti atoms in LTP by various trivalent, tetravalent and pentavalent cations  $\times$  (LXTP) leads to structural changes, thus affecting Li mobility. The minimum energy path (MEP) of the Li jump between adjacent M1 sites is obtained by the nudged elastic band (NEB) method (as shown in Figure 14d), and the calculated activation energy of the migration vacancy is between 0.29 eV and 0.75 eV, which is related to the size of the  $\text{LiO}_6$  octahedron in the structure. Figure 14e/f further shows that the structures with a vacant Li position inside a larger polyhedron are more stable, this is because O atoms bind the  $\text{Li}^+$  ion more tightly in smaller polyhedral cages than in larger ones due to the  $1/r$  dependence of the electrostatic Coulomb interaction. Shin et al.<sup>[118]</sup> demonstrated that the multi-doping of additional Ta

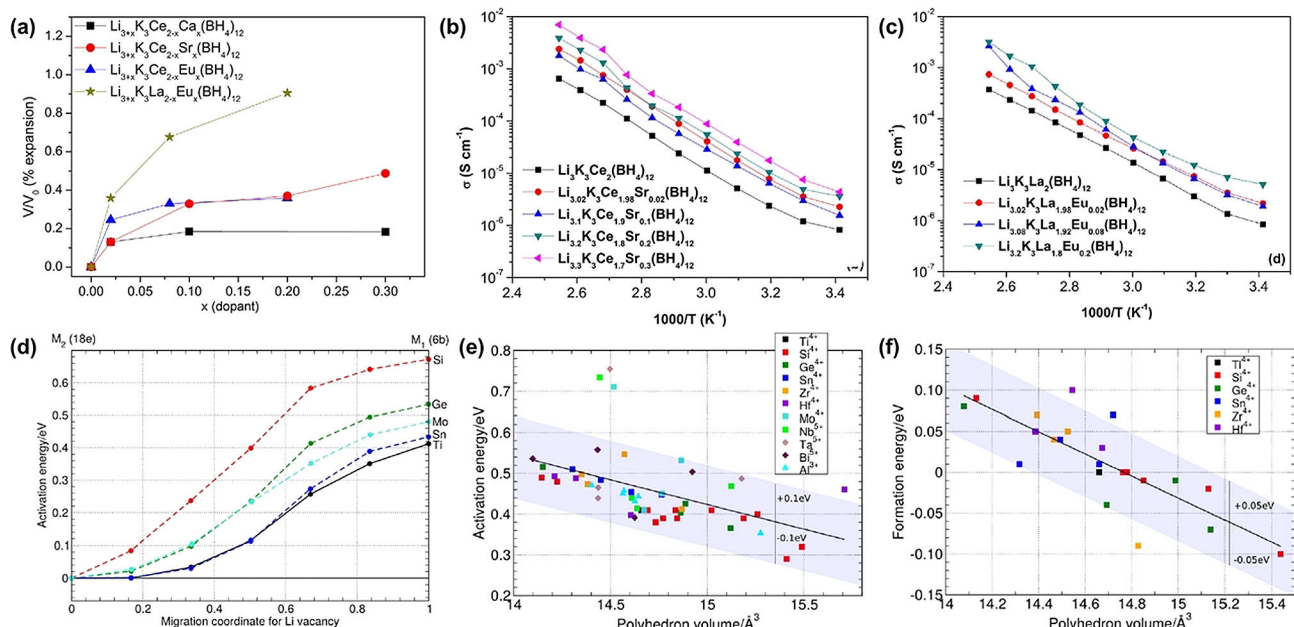


**Figure 14.** (a) Doping concentration dependence of unit cell volume for  $\text{Li}_3\text{K}_3\text{Ce}_2(\text{BH}_4)_{12}$  and  $\text{Li}_3\text{K}_3\text{La}_2(\text{BH}_4)_{12}$ , for divalent cation substitution. (b)/(c) Temperature dependency of Li-ionic conductivity over a range  $293 \leq T \leq 393$  K for the divalent doped samples.  $\sigma$  is shown for  $\text{Li}_3\text{K}_3\text{Ce}_2(\text{BH}_4)_{12}$  doped with  $\text{Sr}^{2+}/\text{Eu}^+$ .<sup>[117]</sup> Reprinted (adapted) with permission from ref. 117. Copyright (2016) Elsevier. (d) MEPs of the migration path of a Li vacancy in  $\text{LiX}_2(\text{PO}_4)_3$ ,  $\text{X}=\text{Si}, \text{Ge}, \text{Sn}, \text{Ti}$ , and  $\text{Mo}$ . (e) / (f) Activation (left) and formation energies (right, relative to LTP) against the polyhedra volumes of  $\text{LiO}_6$  octahedra in  $\text{LiX}_{0.2}\text{Ti}_{1.8}(\text{PO}_4)_3$ .<sup>[102]</sup> Reprinted (adapted) with permission from ref. 102. Copyright (2015) American Chemical Society.

dopants in Al-doped LLZO shifts the most energetic favorable position of Al in the crystal structure from 24 d to 96 h Li sites, thereby it provides more open space for Li ion transportation. This synergistic effect makes the ion conductivity ( $6.14 \times 10^{-4} \text{ S cm}^{-1}$ ) of multi-doped LLZO approximately three times higher than that of single-doped LLZO. The substitution of elements can affect the lattice volume, while the direct doping of compounds can also significantly modify the ion conduction behavior. For example, Subbu et al.<sup>[119]</sup> observed the improvement of ionic conductivity in polymer electrolytes prepared by complexation of lithium salts with polyethylene oxide (PEO) and polyvinylidene chloride-co-acrylonitrile (PVdC-co-AN), and among the various lithium salts studied, the lithium trifluoromethanesulfonate [ $\text{LiN}(\text{CF}_3\text{SO}_2)_2$ ]-based electrolyte exhibits the highest ionic conductivity at room temperature of  $0.265 \times 10^{-5} \text{ S cm}^{-1}$ . Iranipour et al.<sup>[120]</sup> recently reported studies on the equilibrium phase behavior and the effect of lithium salt (lithium tetrafluoroborate) on the organic ionic plastic crystal (OIPC), N-ethyl-N-methylpyrrolidinium tetrafluoroborate [ $\text{C}_2\text{mpyr}$ ]  $[\text{BF}_4^-]$ . In addition to the equilibrium phase transformations of the pure OIPC, new transitions are observed after the addition of the lithium salt (10 mol% and 20 mol%  $\text{LiBF}_4$ ), which significantly alters the ion conduction behavior of the material. The doping of these polymers usually has an important relationship with their concentration, but due to the lack of systematic theoretical research on the conduction in polymers, further exploration of its influencing factors is needed.

In addition to the doping of elements, the preparation of composite materials from two or more materials is also an effective way to improve the ion conduction. For example,

coating cathode materials such as  $\text{LiCoO}_2$ ,  $\text{LiFePO}_4$  with carbon<sup>[121]</sup> effectively improves the electrical conductivity of the materials and suppressing the occurrence of side reactions with the electrolyte. In solid-state electrolytes, compositing metal oxide nanoparticles ( $\text{TiO}_2$ ,  $\text{Al}_2\text{O}_3$ ,  $\text{SiO}_2$ ) with polymers or inorganic materials is a common method.<sup>[122]</sup> Choi et al.<sup>[123]</sup> reported the synthesis of a fast solid Li-ion conductor composed of  $\text{LiBH}_4$  and  $\text{SiO}_2$  through interface engineering, which exhibits extremely high ionic conductivity of  $\sim 10^{-4} \text{ S cm}^{-1}$  at room temperature. The volume fraction and specific surface area (or particle size) of the insulating phase determine the reinforcing effect because they change the proportion of the interface layer with high ion conductivity. The activation energy of  $\text{LiBH}_4$ -fumed silica mixture (LF 55 vol% composite) reached 0.43 eV (Figure 15a), which is much lower than the activation energy of pure  $\text{LiBH}_4$ , reflecting the faster Li ion conduction through the interface layer. Choi et al.<sup>[124]</sup> investigated morphology, ion conduction, and dielectric response of polysiloxane-based single-ion conductors containing weak-binding borates and cyclic carbonate side chains mixed with plasticizing PEG600. The result shows that as PEG600 is added, not only lower activation energy  $E_a$  and higher ionic conductivity (Figure 15b), but also higher mobility and lower fragility is obtained. Suggesting an increase in polymer chain flexibility by decreasing  $T_g$ , after mixing LiPSBC with propylene carbonate ( $\varepsilon = 65$  at  $25^\circ\text{C}$ ), the conductivity was boosted by over  $10000 \times (\sigma_{DC} \sim 10^{-4} \text{ S cm}^{-1}$  at  $25^\circ\text{C}$ ).

Previous reports have pointed out the influence of the composite interface on ion conduction, but there are rarely thorough theoretical calculations to explore the interaction and

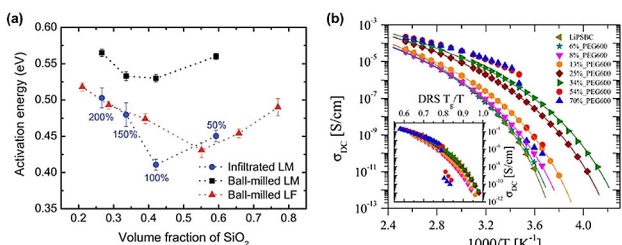


**Figure 15.** (a) Activation energy of Li ion conduction in the infiltrated LM, ballmilled LM, and ball-milled LF mixtures as a function of volume fraction of  $\text{SiO}_2$ . For the infiltrated LM mixtures, the same  $x$  values as the ball-milled LM mixtures are used for convenience, and the corresponding mixing ratios (200, 150, 100 and 50%) are annotated.<sup>[123]</sup> Reprinted (adapted) with permission from ref. 123. Copyright (2016) Royal Society of Chemistry. (b) Temperature dependence of ionic conductivity for LiPSBC and its blends with PEG600 (and vs DRS  $T_g/T$  in the inset).<sup>[124]</sup> Reprinted (adapted) with permission from ref. 124. Copyright (2014) American Chemical Society.

conduction mechanism occurring at the interface. Fu et al.<sup>[125]</sup> recently reported an work in this area, in which they proposed a new biotechnology to fabricate novel protein-ceramic hybrid nanofillers. The specific method is to coat the ion-conductive soy protein onto the  $\text{TiO}_2$  nanoparticles by a controlled denaturation process under appropriate solvents and conditions, and as a result, it is found that the ionic conductivity is increased from  $5 \times 10^{-6}$  to  $6 \times 10^{-5} \text{ S cm}^{-1}$  at room temperature. To further understand what is happening on the interfaces of this composite, molecular simulations are performed to study the chain configuration and protein/ $\text{TiO}_2$  interactions. As shown in Figure 16, relative to  $\text{TiO}_2$ /(SP-close) hybrid (Figure 16a), strong and stable absorption of SP onto  $\text{TiO}_2$  nanoparticles in the  $\text{TiO}_2$ /(SP-open) hybrid (Figure 16b) is observed. Based on the implementation and simulation results, they propose a model (Figure 16c) to explain that the presence of  $\text{TiO}_2$  promotes the denaturation of SP and the exposure of protein functional groups. As a result, the denatured SPs strongly bind to the  $\text{TiO}_2$  surface and form a stable SP coating. Meanwhile, the functional groups on protein coating also actively interact with the polymer matrix, leading to improved mechanical strength and flexibility. For how the  $\text{TiO}_2$ /(SP-open) hybrid nanofillers help the ion transportation inside the CPEs, the denatured proteins on the  $\text{TiO}_2$ /SP hybrid nanofillers may form unique ionic pathways, depending on the protein configuration, as revealed in this study. More specifically, the ion transport is very different because of the distinction of protein configuration structures on the  $\text{TiO}_2$  surfaces, and the protein/PEO- $\text{Li}^+$  interactions may also significantly contribute to the ion conduction. The regulation of lattice and interface engineering can significantly improve the ion conduction behavior of materials. The latest research reports mentioned above show its great potential in these areas, and more importantly, it is necessary to conduct theoretical research and simulation on the deeper causes of the appearance to further guide the experimental exploration.

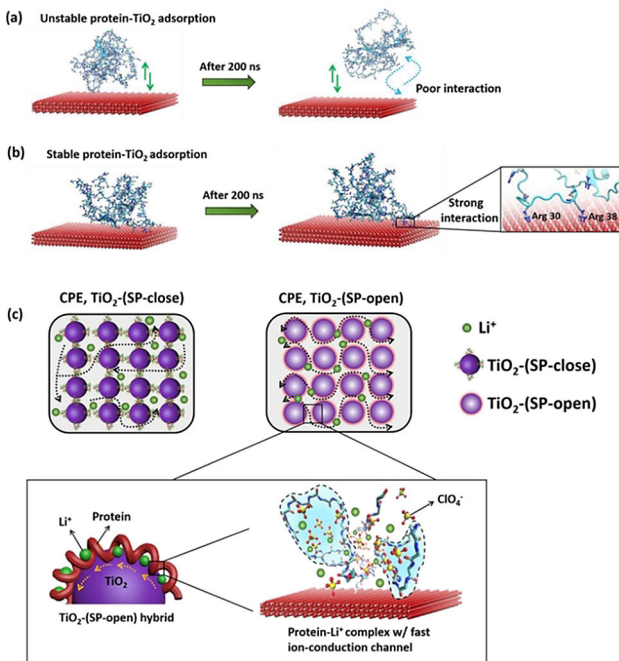


**Figure 16.** Simulation studies on the interactions between denatured SP and  $\text{TiO}_2$  nanoparticles. (a) Weak and unstable absorption of SP onto  $\text{TiO}_2$  nanoparticles in the  $\text{TiO}_2$ /(SP-close) hybrid; (b) strong and stable absorption of SP onto  $\text{TiO}_2$  nanoparticles in the  $\text{TiO}_2$ /(SP-open) hybrid; (c) schematics of the fast ion-conduction channel formed in the  $\text{TiO}_2$ /(SP open) hybrid and ion transport pathways in CPEs with the  $\text{TiO}_2$ /(SP open) hybrid compared with the  $\text{TiO}_2$ /(SP close) hybrid.<sup>[125]</sup> Reprinted (adapted) with permission from ref. 125. Copyright (2018) American Chemical Society.

### 3.3.3. Experimental Synthesis and Modification Methods

In this section, the experimental synthesis and modification methods to improve ion conduction in recent years are investigated. The synthesis methods related to carbon-based anode materials and some new synthetic ideas of electrode materials will be briefly introduced, thereafter, the latest research on the interface between electrolyte and electrode materials and the surface modification of the electrode materials are discussed.

Graphite is one of the most successful commercial anode materials. However, It's limited by the relatively low theoretical capacity ( $372 \text{ mAh g}^{-1}$ ), and leading to increasing demand for alternative anode materials with better alkali metal ion storage capacity. In the past few years, many materials with high theoretical capacity, such as metal oxides, sulfides and selenides, have been studied for specific batteries.<sup>[126]</sup> Recent reports indicate that  $\text{VS}_2$  nanosheet assemblies prepared by solvothermal methods can be used as a general host material for alkali metal ions.<sup>[127]</sup> However, such materials tend to have poor cycle performance due to large volume expansion during ion insertion. In order to solve this problem, on the one hand, doping or compounding can be utilized. For example, Niu et al.<sup>[128]</sup> synthesized  $\text{MoSe}_2$  on N, P-codoped carbon nanosheets by solvothermal reaction, and then calcined at high temperature. The combination of N and P into carbon enhances its interaction with active materials during cycling, which greatly

improves the electrochemical performance. On the other hand, many strategies have been developed to construct various complex nanostructures (e.g. hollow, core-shell and porous nanostructures, etc.). For example, Yuan et al.<sup>[129]</sup> used colloidal carbon spheres as a template, and then fabricated SnO<sub>2</sub>/polypyrrole (SnO<sub>2</sub>/PPy) hollow spheres by liquid deposition method which using in-situ chemical polymerization. Yuan et al.<sup>[130]</sup> prepared a core-shell Ni<sub>3</sub>[Co(CN)<sub>6</sub>]<sub>2</sub> @ polydopamine (PDA) nanocube as a precursor, prepared the Nano NiCo<sub>2</sub>S<sub>4</sub> @ C, which is encapsulated in a hollow nitrogen-doped carbon cube (NiCo<sub>2</sub>S<sub>4</sub> @ D-NC). Li et al.<sup>[131]</sup> constructed a unique egg yolk-shell microsphere structure composed of mesoporous cobalt sulfide egg yolk and alveolar carbon shell (M-CoS @ C).

Figure 17 shows some recent experimental synthesis strategies. The solvothermal method followed by calcination is a common method for synthesizing the above metal oxide/sulfide and carbon composites.<sup>[127–128,132]</sup> Figure 17a<sup>[132a]</sup> depicts this typical process. In an autoclave environment with high temperature and high pressure, thiourea gradually releases S<sup>2–</sup>, which can react with Zn<sup>2+</sup> to form ZnS nanocrystals. The glucose molecules in the solution undergo polymerization, condensation and aromatization processes to form a uniform carbon-rich polysaccharide on the surface of the ZnS nanospheres, and followed by calcination in an argon atmosphere to form the desired core-shell ZnS/C nanocomposite. In addition, ultra-thin two-dimensional lamellar materials such as black phosphorus and graphene are also hot research topics as

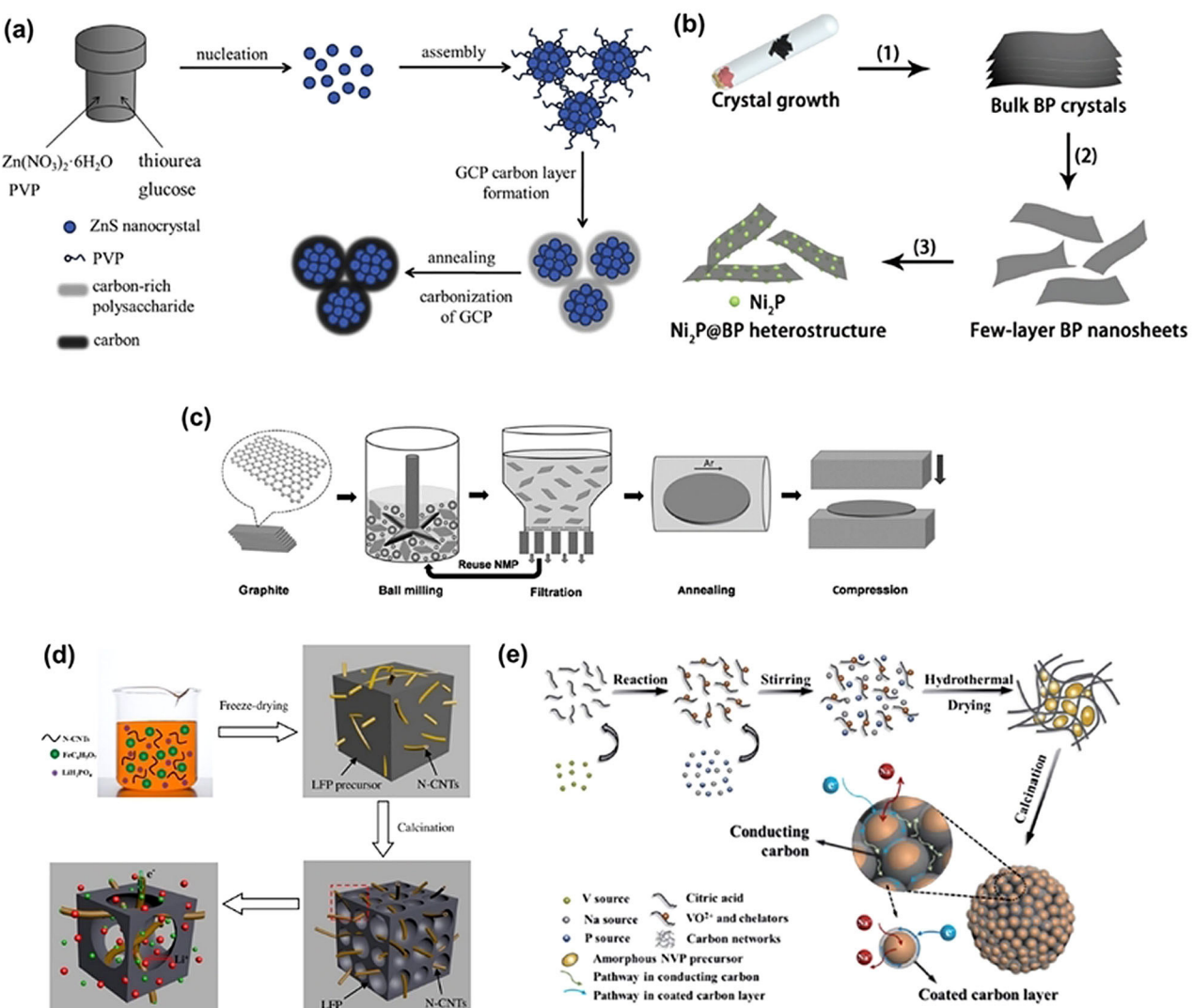


**Figure 17.** Some experimental synthesis strategies: (a) Schematic illustration of the formation of the ZnS/C nanocomposite.<sup>[132a]</sup> Reprinted (adapted) with permission from ref. 132a. Copyright (2017) Elsevier. (b) Schematic illustration for the synthesis process of the Ni<sub>2</sub>P@BP heterostructure: (1) chemical vapor transport deposition process, (2) liquid exfoliation, and (3) solvothermal synthesis with NiCl<sub>2</sub>.<sup>[132b]</sup> Reprinted (adapted) with permission from ref. 132b. Copyright (2016) John Wiley & Sons. (c) Preparation process of graphene paper from graphite.<sup>[133]</sup> Reprinted (adapted) with permission from ref. 133. Copyright (2017) John Wiley & Sons. (d) Schematic illustration of the synthesis process for the porous LFP/N-CNTs composite.<sup>[135]</sup> Reprinted (adapted) with permission from ref. 135. Copyright (2017) Elsevier. (e) Schematic illustration of the synthetic process and structure of PL-NVP@C.<sup>[136]</sup> Reprinted (adapted) with permission from ref. 136. Copyright (2017) Royal Society of Chemistry.

anode materials. Luo et al.<sup>[132b]</sup> reported the synthesis of 0D transition metal phosphide (TMPs) nanocrystals (NCs)-2D ultra-thin black phosphorus (BP) heterostructure ( $\text{Ni}_2\text{P} @ \text{BP}$ ) by ultrasonic-assisted stripping followed by solvothermal reaction (as shown in Figure 17b). Teng et al.<sup>[133]</sup> reported an effective way to construct ultra-high-conductivity graphene paper. The specific process is shown in Figure 17c. Firstly, the small layer of graphene dispersion with a large volume, high concentration and no planar defects is rapidly produced from graphite by ball milling in high yield. The stripped graphene dispersion is then further processed into graphene paper by rapid filtration, heat treatment and mechanical compression, and the electrical conductivity and thermal conductivity of the resulting graphene paper are as high as  $2231 \text{ S cm}^{-1}$  and  $1529 \text{ W m}^{-1} \text{ K}^{-1}$ , which are better than previous reports. Yang et al.<sup>[134]</sup> also reported the fabrication of LVO/C/CNT composites by using a spray drying process followed by heat treatment in an inertial atmosphere, which has a high specific surface and graded porous structure, and thus exhibits higher  $\text{Li}^+$  ion diffusivity and rate performance.

For the synthesis of cathode materials, in general, reducing the size of particles of common cathode materials such as  $\text{LiFePO}_4$  to the nanometer scale and carbon coating is considered to be effective ways to improve the electrochemical performance. Tu et al.<sup>[135]</sup> successfully prepared uniformly dispersed nitrogen-doped carbon nanotube-modified three-dimensional porous  $\text{LiFePO}_4$  by using freeze-drying method (Figure 17d) instead of traditional synthesis method. The specific step is that the black suspension obtained by mixing the raw materials is immediately frozen with liquid nitrogen, and then placed in a vacuum drying freeze dryer at  $-55^\circ\text{C}$  for 48 hours, and finally the cured precursor is heat-treated to obtain the three-dimensional porous structure. Wang et al.<sup>[136]</sup> reported the use of in-situ grown conductive carbon to obtain a pomegranate-like NVP@C composite by simple sol-gel-assisted hydrothermal techniques (Figure 17e). Unlike commonly used glucose as a carbon source, they use a chelation between vanadate and citric acid to encapsulate the NVP precursor by hydrothermal treatment of the carbon species, followed by high-temperature calcination to produce a pomegranate-structured NVP@C composite. This method can potentially prevent the interconnected framework of NVP aggregation, maximally isolating the active redox surface of the NVP. In addition, the research on using carbon-based materials (e.g. carbon nanotubes, graphene) for flexible energy storage devices is also one of the current hot spots.<sup>[137]</sup> Huisheng Peng and coworkers have conducted in-depth research in this field.<sup>[138]</sup> Recently, they developed an effective method to fabricate highly stretchable supercapacitors with high electrochemical performances by incorporating a family of nitrogen (N)-doped core-sheath carbon nanotube (NCNT) array as an elastic electrode (as shown in Figure 18). It demonstrates a high specific capacitance of  $31.1 \text{ mF cm}^{-2}$  and 98.9% specific capacitance retention at a strain of 400%.

In the studies of solid-state electrolytes, cubic garnet type solid-state electrolytes have been widely researched due to their high ionic conductivity ( $10^{-4}\text{--}10^{-3} \text{ S cm}^{-1}$ )<sup>[143]</sup> and stability

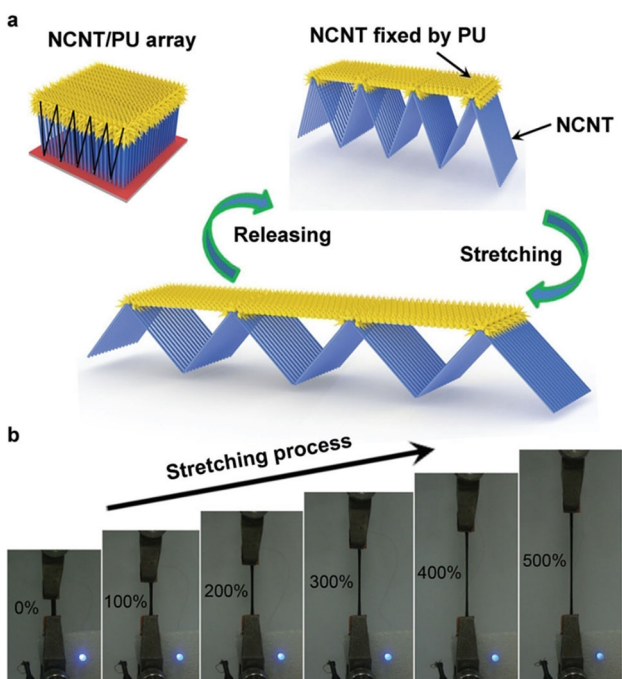


**Figure 18.** (a) Schematic illustration to the stretching mechanism of NCNT/PU film. (b) Photograph of the NCNT/PU film with strain increased from 0 to 500%.<sup>[138c]</sup> Reprinted (adapted) with permission from ref. 138c. Copyright (2017) John Wiley & Sons.

to lithium metal up to  $300^\circ\text{C}$ . However, due to the rigidity of garnet and its high stability to lithium metal, its wettability to molten lithium is poor, which affects the contact between garnet SSE and lithium metal, and results in large polarized and uneven ions flowing through the interface. To solve this problem, Zhou et al.<sup>[144]</sup> proposed the introduction of cross-linked polymers between garnet and lithium metal, which effectively improved their contact and provided stable electrochemical cycling performance. However, the volumetric energy density of the battery is also limited by this thick polymer interlayer. Basappa et al.<sup>[145]</sup> studied the charge transfer resistance between lithium metal and LLZT using LLZT pellets with various roughness, and successfully reduced the interfacial resistance by polishing the LLZT particles. On this basis, the deposition of the lithium metal on the LLZT particles by vacuum evaporation further increases the contact area. Luo et al.<sup>[139]</sup> also proposed a new method for reducing the interfacial resistance of garnet/lithium metal by evaporation of a thin layer of germanium (Ge) (20 nm) on garnet (as shown in Figure 19a). Due to the alloying reaction between Li and Ge, the garnet/Li-metal interface resistance is reduced from about 900 to about  $115 \Omega \text{ cm}^2$ . Wang et al.<sup>[140]</sup> used an ultra-thin ZnO surface coating prepared by atomic layer deposition (ALD) to improve the wettability of garnet solid electrolyte to molten lithium (as shown in Figure 19b), thereby significantly reducing the interfacial resistance to as low as  $20 \Omega \text{ cm}^2$ . The works mentioned above shows a significant breakthrough in garnet type SSE interface resistance, and provides a new way for other similar interface problems.

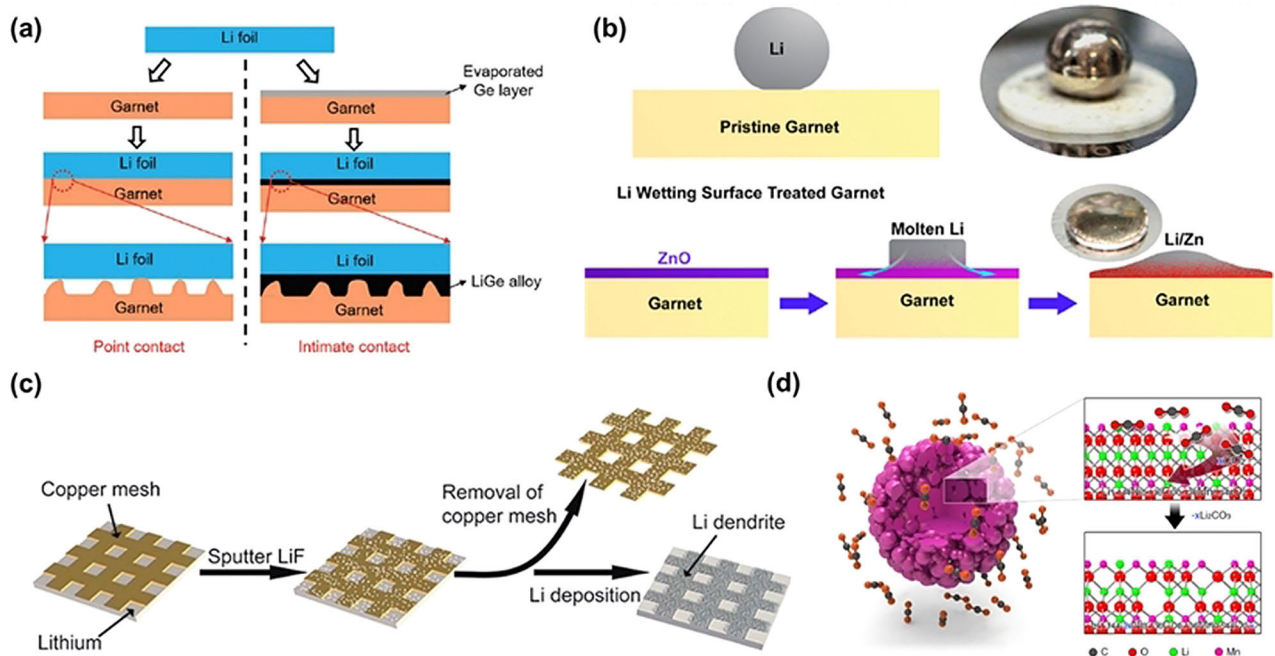


**Figure 19.** (a) Schematic representation for improving the contact between garnet and Li metal by engineering the surface of the garnet with a thin Ge layer.<sup>[139]</sup> Reprinted (adapted) with permission from ref. 139. Copyright (2017) John Wiley & Sons. (b) Schematic of surface-treated garnet wetted with molten lithium.<sup>[140]</sup> Reprinted (adapted) with permission from ref. 140. Copyright (2017) American Chemical Society. (c) Schematic illustration of preparing patterned LiF-coated Li metal anode and Li deposition on patterned LiF-coated Li metal anode.<sup>[141]</sup> Reprinted (adapted) with permission from ref. 141. Copyright (2017) Royal Society of Chemistry. (d) Schematic of GSIR between Li-rich layered oxides and carbon dioxide.<sup>[142]</sup> Reprinted (adapted) with permission from ref. 142. Copyright (2016) Springer Nature.

In the studies of interfacial modification of electrode materials, the formation of an unstable solid electrolyte interphase (SEI) on the surface of the material and subsequent nucleation of the lithium electroformation is a key issue to limit the progress in this field. In general, on the one hand, by introducing new electrolyte system and additives, the SEI stability can be enhanced.<sup>[146]</sup> On the other hand, surface coating technologies are important methods for stabilizing Li metal anode. For example, the Chemical/Physical vapor deposition (CVD/PVD), Atomic layer deposition (ALD) etc.<sup>[147]</sup> These coatings serve to protect the cathode material from undesirable side reactions with the electrolytes, thereby reduce electrolyte decomposition to attenuate the SEI layer for improving cycle performance. Fan et al.<sup>[141]</sup> reported a new strategy for establishing a uniform SEI layer by magnetron sputtering on a lithium anode to promote uniform lithium electrodeposition. The deposition process is shown in Figure 19c. The electrode obtained from the battery with the modified Li anode shows stable lithium deposition, and DFT simulations show that artificial SEI rich in lithium fluoride (LiF) salts provide a low energy barrier for the diffusion of lithium ions, and they point out that this novel strategy can be universally applied to other metals such as Na, Al and Zn. In addition, another strategy to inhibit the growth of Li dendrite is to replace Li metal anode with Li alloy or Si/Li–Si anode.<sup>[148]</sup>

In addition to the methods mentioned above, it's also an important method to modify the surface layer of the material itself. Many studies exemplify the contributions of bulk and

surface oxygen on high charge-discharge capacity in Li-rich layered oxides.<sup>[149]</sup> Recently, Qiu et al.<sup>[142]</sup> reported the design of gas-solid interface reactions. They proposed a strategy based on gas-solid interface reaction (GSIR) between lithium-rich layered oxide and carbon dioxide gas (as shown in Figure 19d) to generate oxygen vacancies on the surface of the particles, thereby achieving fine control of oxygen activity. Theoretical calculations and experimental characterization indicate that oxygen vacancies provide a favorable ion diffusion environment in the body and significantly inhibit the release of gases from the surface. This study reveals the comprehensive design and control of oxygen activity in transition metal oxide systems for next-generation lithium-ion batteries.

#### 4. Concluding Remarks and Perspectives

In this review, recent studies on ion conduction of AMIBs were investigated. In all-solid-state electrolytes, recent studies have shown that the ionic conductivity of each structure family has been greatly improved compared to previous reports, and the average level has reached  $10^{-3} \text{ Scm}^{-1}$ . Studies of sulfide families have shown their potential for further breakthroughs in higher ionic conductivity. Through simulation calculation combined with experimental research, the influence of crystal structure and grain boundary on diffusion pathway and migration barrier are reported. Element doping and material compounding methods have been widely used to effectively improve the ion

diffusion performance of materials. Essentially, they improve the ion conductivity by changing the lattice parameters of the material and the properties of the interface. In terms of experimental synthesis, the latest material synthesis methods for the preparation of high-performance battery materials are reported, and the unique strategy to construct various complex nanostructures (hollow, core-shell and porous nanostructures, etc.) is also a direction to further improve the performance.

All-solid-state electrolytes, due to their widely recognized safety and mechanical properties, remain the focus of latest studies. As an ideal alternative to liquid electrolytes, ionic conductivity is the prerequisite for evaluating its performance. Although some solid-state electrolytes such as  $\text{Li}_{10}\text{GeP}_2\text{S}_{12}$  have been reported to have ionic conductivity close to liquid electrolytes, it is still insufficient for successful commercial applications. Moreover, the interface problem between the solid-state electrolyte and the electrode material still exists. Relevant studies have made some progress, but it still cannot solve this problem fundamentally. It's necessary to further understand the reaction mechanisms at the interface and develop reliable methods for stabilizing these interfaces. The development of solid-state electrolytes with high safety and high energy density will further promote the future development of Li-S and Li-air batteries.

We believe that the current theoretical research and simulation calculations of ion conduction have made great progress, and put forward many new insights on its related influencing factors, and how to combine it with experimental synthesis to solve the current problems is the key. All-solid-state electrolytes will be the key to the successful application of the next generation of alkali metal-ion batteries, and understanding the ion conduction phenomenon is extremely important, which indicates the great potential and bright prospects in this field.

## Acknowledgements

This work was supported by the Shenzhen Science and Technology Research Grant (JCYJ20170412150450297), the National Natural Science Foundation of China (21622407, 21875266) and the Strategic Priority Research Program of the Chinese Academy of Sciences (XDA21010214).

## Conflict of Interest

The authors declare no conflict of interest.

**Keywords:** alkali metal-ion batteries • ion conduction • ionic conductivity • ionic diffusivity • power sources

- [1] a) M. Armand, J. M. Tarascon, *Nature* **2008**, *451*, 652–657; b) J. M. Tarascon, M. Armand, *Nature* **2001**, *414*, 359–367.
- [2] K. Kubota, M. Dahbi, T. Hosaka, S. Kumakura, S. Komaba, *Chem. Rec.* **2018**, *18*, 459–479.
- [3] S. Moore, M. Ehsani, *Advances in Electric Vehicle Technology*, SAE, **1999**.

- [4] a) M. S. Whittingham, *Science* **1976**, *192*, 1126–1127; b) K. Mizushima, P. C. Jones, P. J. Wiseman, J. B. Goodenough, *Mater. Res. Bull.* **1980**, *15*, 783–789; c) A. K. Padhi, K. S. Nanjundaswamy, J. B. Goodenough, *J. Electrochem. Soc.* **1997**, *144*, 1188–1194.
- [5] C. P. Hunt, B. M. Moskowitz, B. S. K. *Physical properties of rocks and minerals*, CRC Press, Boca Raton, **1989**.
- [6] a) J. F. Whitacre, A. Tevar, S. Sharma, *Electrochem. Commun.* **2010**, *12*, 463–466; b) M. Jacoby, *Chem. Eng. News* **2017**, *95*, 11–11; c) Z. Jian, Z. Xing, C. Bommier, Z. Li, X. Ji, *Adv. Energy Mater.* **2016**, *6*, 1501874; d) T. Shao, C. Li, C. Liu, W. Deng, W. Wang, M. Xue, R. Li, *J. Mater. Chem. A* **2019**, *7*, 1749–1755; e) W. Deng, X. Wang, C. Liu, C. Li, J. Chen, N. Zhu, R. Li, M. Xue, *Energy Storage Mater.* **2018**.
- [7] a) S. Komaba, T. Hasegawa, M. Dahbi, K. Kubota, *Electrochem. Commun.* **2015**, *60*, 172–175; b) M. Okoshi, Y. Yamada, S. Komaba, A. Yamada, H. Nakai, *J. Electrochem. Soc.* **2017**, *164*, A54–A60.
- [8] Z. Jian, W. Luo, X. Ji, *J. Am. Chem. Soc.* **2015**, *137*, 11566–11569.
- [9] D. Linden, *Handbook of Batteries*, 3rd edition ed., McGraw-Hill, **2002**.
- [10] a) M. Winter, R. J. Brodd, *Chem. Rev.* **2004**, *104*, 4245–4269; b) M. Kaneko, M. Nakayama, Y. Wakizaka, K. Kanamura, M. Wakihara, *Electrochim. Acta* **2008**, *53*, 8196–8202.
- [11] a) C. Y. Wang, X. Zhang, *Current Opinion in Solid State & Materials Science* **2006**, *10*, 2–14; b) J. Hafner, C. Wolverton, G. Ceder, *MRS Bull.* **2006**, *31*, 659–665; c) Y. Meng, M. Arroyo-de Dompablo, *Energy Environ. Sci.* **2009**, *2*, 589–609; d) F. Zhou, M. Coccioni, C. A. Marianetti, D. Morgan, G. Ceder, *Phys. Rev. B* **2004**, *70*, 235121; e) C. Y. Ouyang, S. Q. Shi, Z. X. Wang, H. Li, X. J. Huang, L. Q. Chen, *Journal of Physics-Condensed Matter* **2004**, *16*, 2265–2272; f) K. Hoang, M. D. Johannes, *J. Power Sources* **2012**, *206*, 274–281.
- [12] L. Wang, T. Maxisch, G. Ceder, *Chem. Mater.* **2007**, *19*, 543–552.
- [13] a) C. Y. Ouyang, S. Q. Shi, Z. X. Wang, X. J. Huang, L. Q. Chen, *Phys. Rev. B* **2004**, *69*, 104303; b) Y. Sun, X. Lu, R. Xiao, H. Li, X. Huang, *Chem. Mater.* **2012**, *24*, 4693–4703; c) J. Yang, J. S. Tse, *J. Phys. Chem. A* **2011**, *115*, 13045–13049.
- [14] K. Xu, *Chem. Rev.* **2014**, *114*, 11503–11618.
- [15] a) K. Xu, *Chem. Rev.* **2004**, *104*, 4303–4417; b) E. L. Cussler, *Diffusion*, Cambridge University Pres, **1984**; c) D. S. Wilkinson, *Mass Transport in Solid and Fluids*, Cambridge University Press, **2000**; d) D. A. Porter, K. E. Easterling, *Phase Transformations in Metals and Alloys*, 2nd edition ed., Chapman & Hall, **1992**.
- [16] F. Croce, A. Daprano, C. Nanjundiah, V. R. Koch, C. W. Walker, M. Salomon, *J. Electrochem. Soc.* **1996**, *143*, 154–159.
- [17] a) K. Xu, C. A. Angell, *Electrochim. Acta* **1995**, *40*, 2401–2403; b) S. S. Zhang, G. X. Wan, *J. Appl. Polym. Sci.* **1993**, *48*, 405–409; c) Y. Tada, M. Sato, N. Takeno, Y. Nakacho, K. Shigehara, *Chem. Mater.* **1994**, *6*, 27–30.
- [18] H. G. Schweiger, M. Multerer, M. Schweizer-Berberich, H. J. Gores, *J. Electrochem. Soc.* **2005**, *152*, A577–A582.
- [19] M. S. Ding, K. Xu, S. S. Zhang, K. Amine, G. L. Henriksen, T. R. Jow, *J. Electrochem. Soc.* **2001**, *148*, A1196–A1204.
- [20] a) M. S. Ding, T. R. Jow, *J. Electrochem. Soc.* **2003**, *150*, A620–A628; b) Y. Choquette, G. Brisard, M. Parent, *J. Electrochem. Soc.* **1998**, *145*, 3500–3507.
- [21] Y. Matsuda, H. Nakashima, M. Morita, Y. Takasu, *J. Electrochem. Soc.* **1981**, *128*, 2552–2556.
- [22] J. Landesfeind, M. Graf, M. Dahbi, K. Kubota, S. Komaba, H. A. Gasteiger, *Meeting Abstracts* **2017**, MA2017-01, 211.
- [23] H. Mehrer, *Diffusion in Solids*, Springer, **2007**.
- [24] a) R. P. Buck, *Sens. Actuators* **1981**, *1*, 137–196; b) J. B. Goodenough, *Annu. Rev. Mater. Res.* **2003**, *33*, 91–128.
- [25] J. C. Bachman, S. Muy, A. Grimaud, H.-H. Chang, N. Pour, S. F. Lux, O. Paschos, F. Maglia, S. Lupart, P. Lamp, L. Giordano, Y. Shao-Horn, *Chem. Rev.* **2016**, *116*, 140–162.
- [26] R. Tarneberg, A. Lunden, *Solid State Ionics* **1996**, *90*, 209–220.
- [27] J. T. Kummer, *Prog. Solid State Chem.* **1972**, *7*, 141–175.
- [28] V. A. Nikitina, S. S. Fedotov, S. Y. Vassiliev, A. S. Samarin, N. R. Khasanova, E. V. Antipov, *J. Electrochem. Soc.* **2017**, *164*, A6373–A6380.
- [29] a) R. S. Nicholson, I. Shain, *Anal. Chem.* **1964**, *36*, 706–723; b) C. J. Wen, B. A. Boukamp, R. A. Huggins, W. Weppner, *J. Electrochem. Soc.* **1979**, *126*, 2258–2266; c) Q. Wang, H. Li, X. J. Huang, L. Q. Chen, *J. Electrochem. Soc.* **2001**, *148*, A737–A741; d) C. Ho, I. D. Raistrick, R. A. Huggins, *J. Electrochem. Soc.* **1980**, *127*, 343–350.
- [30] Y. Zhu, T. Gao, X. Fan, F. Han, C. Wang, *Acc. Chem. Res.* **2017**, *50*, 1022–1031.
- [31] S. R. Das, S. B. Majumder, R. S. Katiyar, *J. Power Sources* **2005**, *139*, 261–268.

- [32] H. Kanoh, Q. Feng, T. Hirotsu, K. Ooi, *J. Electrochem. Soc.* **1996**, Medium: X; Size: pp. 2610–2615.
- [33] P. Hohenberg, W. Kohn, *Phys. Rev. B* **1964**, *136*, 864–871.
- [34] a) W. Kohn, L. J. Sham, *Phys. Rev.* **1965**, *140*, 1133–1138; b) J. C. Slater, *Phys. Rev.* **1951**, *81*, 385–390.
- [35] a) D. C. Langreth, J. P. Perdew, *Phys. Rev. B* **1980**, *21*, 5469–5493; b) R. McWeeny, *Rev. Mod. Phys.* **1960**, *32*, 335–369.
- [36] A. Jain, Y. Shin, K. A. Persson, *Nat. Rev. Mater.* **2016**, *1*, 15004.
- [37] G. Kresse, J. Furthmüller, *Phys. Rev. B* **1996**, *54*, 11169–11186.
- [38] A. Van der Ven, J. C. Thomas, Q. Xu, B. Swoboda, D. Morgan, *Phys. Rev. B* **2008**, *78*, 104306.
- [39] S. Yamakawa, H. Yamasaki, T. Koyama, R. Asahi, *J. Power Sources* **2013**, *223*, 199–205.
- [40] Y. Ma, S. H. Garofalini, *J. Am. Chem. Soc.* **2012**, *134*, 8205–8211.
- [41] a) T. V. S. L. Satyavani, B. Ramya Kiran, V. Rajesh Kumar, A. Srinivas Kumar, S. V. Naidu, *Engineering Science and Technology, an International Journal* **2016**, *19*, 40–44; b) Y. Ren, P. Lu, X. Huang, S. Zhou, Y. Chen, B. Liu, F. Chu, J. Ding, *Solid State Ionics* **2015**, *274*, 83–87; c) C. Zhang, H. Song, C. Liu, Y. Liu, C. Zhang, X. Nan, G. Cao, *Adv. Funct. Mater.* **2015**, *25*, 3497–3504; d) C. Ding, Y. Zeng, L. Cao, L. Zhao, Y. Zhang, *J. Mater. Chem. A* **2016**, *4*, 5989–5908; e) H. Li, X. Yu, Y. Bai, F. Wu, C. Wu, L.-Y. Liu, X.-Q. Yang, *J. Mater. Chem. A* **2015**, *3*, 9578–9586; f) J. Han, Y. Niu, S. J. Bao, Y. N. Yu, S. Y. Lu, M. Xu, *Chem. Commun.* **2016**, *52*, 11661–11664; g) Y. Cheng, J. Huang, J. Li, Z. Xu, L. Cao, H. Ouyang, J. Yan, H. Qi, *J. Alloys Compd.* **2016**, *658*, 234–240; h) Z. Lin, W. Zhu, Z. Wang, Y. Yang, Y. Lin, Z. Huang, *J. Alloys Compd.* **2016**, *687*, 232–239.
- [42] a) M. V. Reddy, R. Jose, A. Le Viet, K. I. Ozoemena, B. V. R. Chowdari, S. Ramakrishna, *Electrochim. Acta* **2014**, *128*, 198–202; b) J.-H. Jeong, D.-w. Jung, E. W. Shin, E.-S. Oh, *J. Alloys Compd.* **2014**, *604*, 226–232; c) C. Chen, Y. Dong, S. Li, Z. Jiang, Y. Wang, L. Jiao, H. Yuan, *J. Power Sources* **2016**, *320*, 20–27; d) R. Liu, D. Li, C. Wang, N. Li, Q. Li, X. Lü, J. S. Spendelow, G. Wu, *Nano Energy* **2014**, *6*, 73–81; e) C. Liu, C. Zhang, H. Song, C. Zhang, Y. Liu, X. Nan, G. Cao, *Nano Energy* **2016**, *22*, 290–300; f) M.-C. Kim, S.-J. Kim, S.-B. Han, D.-H. Kwak, E.-T. Hwang, D.-M. Kim, G.-H. Lee, H.-S. Choe, K.-W. Park, *J. Mater. Chem. A* **2015**, *3*, 23003–23010; g) C. Nithya, *ChemPlusChem* **2015**, *80*, 1000–1006.
- [43] Y. Dong, Y. Zhao, H. Duan, P. Singh, Q. Kuang, H. Peng, *J. Power Sources* **2016**, *319*, 104–110.
- [44] L. Wu, Y. Hu, X. Zhang, J. Liu, X. Zhu, S. Zhong, *J. Power Sources* **2018**, *374*, 40–47.
- [45] a) X. Jiang, H. Liu, J. Song, C. Yin, H. Xu, *J. Mater. Chem. A* **2016**, *4*, 16205–16212; b) M. Omarova, A. Koishybay, N. Yesibolati, A. Mentbayeva, N. Umirov, K. Ismailov, D. Adair, M.-R. Babaa, I. Kurmanbayeva, Z. Bakunov, *Electrochim. Acta* **2015**, *184*, 58–63.
- [46] Y. Zou, X. Yang, C. Lv, T. Liu, Y. Xia, L. Shang, G. I. Waterhouse, D. Yang, T. Zhang, *Adv Sci (Weinh)* **2017**, *4*, 1600262.
- [47] a) J. Li, N. J. Dudney, X. Xiao, Y.-T. Cheng, C. Liang, M. W. Verbrugge, *Adv. Energy Mater.* **2015**, *5*, 1401627; b) J. Kaspar, M. Graczyk-Zajac, R. Riedel, *Electrochim. Acta* **2014**, *115*, 665–670.
- [48] S. J. R. Prabakar, J. Jeong, M. Pyo, *Electrochim. Acta* **2015**, *161*, 23–31.
- [49] C. Chen, Y. Huang, H. Zhang, X. Wang, G. Li, Y. Wang, L. Jiao, H. Yuan, *J. Power Sources* **2015**, *278*, 693–702.
- [50] Y. Tao, K. Rui, Z. Wen, Q. Wang, J. Jin, T. Zhang, T. Wu, *Solid State Ionics* **2016**, *290*, 47–52.
- [51] X. Xu, J. Liu, R. Hu, J. Liu, L. Ouyang, M. Zhu, *Chemistry* **2017**, *23*, 5198–5204.
- [52] W. Song, X. Ji, Z. Wu, Y. Yang, Z. Zhou, F. Li, Q. Chen, C. E. Banks, *J. Power Sources* **2014**, *256*, 258–263.
- [53] Y. Dong, S. Li, K. Zhao, C. Han, W. Chen, B. Wang, L. Wang, B. Xu, Q. Wei, L. Zhang, X. Xu, L. Mai, *Energy Environ. Sci.* **2015**, *8*, 1267–1275.
- [54] B. V. R. Reddy, R. Ravikumar, C. Nithya, S. Gopukumar, *J. Mater. Chem. A* **2015**, *3*, 18059–18063.
- [55] G. Ma, K. Huang, J.-S. Ma, Z. Ju, Z. Xing, Q.-c. Zhuang, *J. Mater. Chem. A* **2017**, *5*, 7854–7861.
- [56] Y. W. Lee, D. M. Kim, S. J. Kim, M. C. Kim, H. S. Choe, K. H. Lee, J. I. Sohn, S. N. Cha, J. M. Kim, K. W. Park, *ACS Appl. Mater. Interfaces* **2016**, *8*, 7022–7029.
- [57] a) F. Chen, J. Li, Y. Zhang, D. Yang, Q. Shen, L. Zhang, Springer International Publishing, Cham, **2017**, pp. 115–123; b) C. Shao, Z. Yu, H. Liu, Z. Zheng, N. Sun, C. Diao, *Electrochim. Acta* **2017**, *225*, 345–349; c) S. Qin, X. Zhu, Y. Jiang, M. e. Ling, Z. Hu, J. Zhu, *Appl. Phys. Lett.* **2018**, *112*, 113901; d) A. Wachter-Welzl, J. Kirowitz, R. Wagner, S. Smetaczek, G. C. Brunauer, M. Bonta, D. Rettenwander, S. Taibl, A. Limbeck, G. Amthauer, J. Fleig, *Solid State Ionics* **2018**, *319*, 203–208; e) B. Stanje, D. Rettenwander, S. Breuer, M. Uitz, S. Berendts, M. Lerch, Springer International Publishing, Cham, **2017**, pp. 115–123; f) F. Chen, J. Li, Y. Zhang, D. Yang, Q. Shen, L. Zhang, Springer International Publishing, Cham, **2017**, pp. 115–123; g) F. Chen, J. Li, Y. Zhang, D. Yang, Q. Shen, L. Zhang, Springer International Publishing, Cham, **2017**, pp. 115–123; h) F. Chen, J. Li, Y. Zhang, D. Yang, Q. Shen, L. Zhang, Springer International Publishing, Cham, **2017**, pp. 115–123; i) F. Chen, J. Li, Y. Zhang, D. Yang, Q. Shen, L. Zhang, Springer International Publishing, Cham, **2017**, pp. 115–123; j) F. Chen, J. Li, Y. Zhang, D. Yang, Q. Shen, L. Zhang, Springer International Publishing, Cham, **2017**, pp. 115–123; k) F. Chen, J. Li, Y. Zhang, D. Yang, Q. Shen, L. Zhang, Springer International Publishing, Cham, **2017**, pp. 115–123; l) F. Chen, J. Li, Y. Zhang, D. Yang, Q. Shen, L. Zhang, Springer International Publishing, Cham, **2017**, pp. 115–123; m) F. Chen, J. Li, Y. Zhang, D. Yang, Q. Shen, L. Zhang, Springer International Publishing, Cham, **2017**, pp. 115–123; n) F. Chen, J. Li, Y. Zhang, D. Yang, Q. Shen, L. Zhang, Springer International Publishing, Cham, **2017**, pp. 115–123; o) F. Chen, J. Li, Y. Zhang, D. Yang, Q. Shen, L. Zhang, Springer International Publishing, Cham, **2017**, pp. 115–123; p) F. Chen, J. Li, Y. Zhang, D. Yang, Q. Shen, L. Zhang, Springer International Publishing, Cham, **2017**, pp. 115–123; q) F. Chen, J. Li, Y. Zhang, D. Yang, Q. Shen, L. Zhang, Springer International Publishing, Cham, **2017**, pp. 115–123; r) F. Chen, J. Li, Y. Zhang, D. Yang, Q. Shen, L. Zhang, Springer International Publishing, Cham, **2017**, pp. 115–123; s) F. Chen, J. Li, Y. Zhang, D. Yang, Q. Shen, L. Zhang, Springer International Publishing, Cham, **2017**, pp. 115–123; t) F. Chen, J. Li, Y. Zhang, D. Yang, Q. Shen, L. Zhang, Springer International Publishing, Cham, **2017**, pp. 115–123; u) F. Chen, J. Li, Y. Zhang, D. Yang, Q. Shen, L. Zhang, Springer International Publishing, Cham, **2017**, pp. 115–123; v) F. Chen, J. Li, Y. Zhang, D. Yang, Q. Shen, L. Zhang, Springer International Publishing, Cham, **2017**, pp. 115–123; w) F. Chen, J. Li, Y. Zhang, D. Yang, Q. Shen, L. Zhang, Springer International Publishing, Cham, **2017**, pp. 115–123; x) F. Chen, J. Li, Y. Zhang, D. Yang, Q. Shen, L. Zhang, Springer International Publishing, Cham, **2017**, pp. 115–123; y) F. Chen, J. Li, Y. Zhang, D. Yang, Q. Shen, L. Zhang, Springer International Publishing, Cham, **2017**, pp. 115–123; z) F. Chen, J. Li, Y. Zhang, D. Yang, Q. Shen, L. Zhang, Springer International Publishing, Cham, **2017**, pp. 115–123; aa) F. Chen, J. Li, Y. Zhang, D. Yang, Q. Shen, L. Zhang, Springer International Publishing, Cham, **2017**, pp. 115–123; bb) F. Chen, J. Li, Y. Zhang, D. Yang, Q. Shen, L. Zhang, Springer International Publishing, Cham, **2017**, pp. 115–123; cc) F. Chen, J. Li, Y. Zhang, D. Yang, Q. Shen, L. Zhang, Springer International Publishing, Cham, **2017**, pp. 115–123; dd) F. Chen, J. Li, Y. Zhang, D. Yang, Q. Shen, L. Zhang, Springer International Publishing, Cham, **2017**, pp. 115–123; ee) F. Chen, J. Li, Y. Zhang, D. Yang, Q. Shen, L. Zhang, Springer International Publishing, Cham, **2017**, pp. 115–123; ff) F. Chen, J. Li, Y. Zhang, D. Yang, Q. Shen, L. Zhang, Springer International Publishing, Cham, **2017**, pp. 115–123; gg) F. Chen, J. Li, Y. Zhang, D. Yang, Q. Shen, L. Zhang, Springer International Publishing, Cham, **2017**, pp. 115–123; hh) F. Chen, J. Li, Y. Zhang, D. Yang, Q. Shen, L. Zhang, Springer International Publishing, Cham, **2017**, pp. 115–123; ii) F. Chen, J. Li, Y. Zhang, D. Yang, Q. Shen, L. Zhang, Springer International Publishing, Cham, **2017**, pp. 115–123; jj) F. Chen, J. Li, Y. Zhang, D. Yang, Q. Shen, L. Zhang, Springer International Publishing, Cham, **2017**, pp. 115–123; kk) F. Chen, J. Li, Y. Zhang, D. Yang, Q. Shen, L. Zhang, Springer International Publishing, Cham, **2017**, pp. 115–123; ll) F. Chen, J. Li, Y. Zhang, D. Yang, Q. Shen, L. Zhang, Springer International Publishing, Cham, **2017**, pp. 115–123; mm) F. Chen, J. Li, Y. Zhang, D. Yang, Q. Shen, L. Zhang, Springer International Publishing, Cham, **2017**, pp. 115–123; nn) F. Chen, J. Li, Y. Zhang, D. Yang, Q. Shen, L. Zhang, Springer International Publishing, Cham, **2017**, pp. 115–123; oo) F. Chen, J. Li, Y. Zhang, D. Yang, Q. Shen, L. Zhang, Springer International Publishing, Cham, **2017**, pp. 115–123; pp) F. Chen, J. Li, Y. Zhang, D. Yang, Q. Shen, L. Zhang, Springer International Publishing, Cham, **2017**, pp. 115–123; qq) F. Chen, J. Li, Y. Zhang, D. Yang, Q. Shen, L. Zhang, Springer International Publishing, Cham, **2017**, pp. 115–123; rr) F. Chen, J. Li, Y. Zhang, D. Yang, Q. Shen, L. Zhang, Springer International Publishing, Cham, **2017**, pp. 115–123; ss) F. Chen, J. Li, Y. Zhang, D. Yang, Q. Shen, L. Zhang, Springer International Publishing, Cham, **2017**, pp. 115–123; tt) F. Chen, J. Li, Y. Zhang, D. Yang, Q. Shen, L. Zhang, Springer International Publishing, Cham, **2017**, pp. 115–123; uu) F. Chen, J. Li, Y. Zhang, D. Yang, Q. Shen, L. Zhang, Springer International Publishing, Cham, **2017**, pp. 115–123; vv) F. Chen, J. Li, Y. Zhang, D. Yang, Q. Shen, L. Zhang, Springer International Publishing, Cham, **2017**, pp. 115–123; ww) F. Chen, J. Li, Y. Zhang, D. Yang, Q. Shen, L. Zhang, Springer International Publishing, Cham, **2017**, pp. 115–123; xx) F. Chen, J. Li, Y. Zhang, D. Yang, Q. Shen, L. Zhang, Springer International Publishing, Cham, **2017**, pp. 115–123; yy) F. Chen, J. Li, Y. Zhang, D. Yang, Q. Shen, L. Zhang, Springer International Publishing, Cham, **2017**, pp. 115–123; zz) F. Chen, J. Li, Y. Zhang, D. Yang, Q. Shen, L. Zhang, Springer International Publishing, Cham, **2017**, pp. 115–123; aa) F. Chen, J. Li, Y. Zhang, D. Yang, Q. Shen, L. Zhang, Springer International Publishing, Cham, **2017**, pp. 115–123; bb) F. Chen, J. Li, Y. Zhang, D. Yang, Q. Shen, L. Zhang, Springer International Publishing, Cham, **2017**, pp. 115–123; cc) F. Chen, J. Li, Y. Zhang, D. Yang, Q. Shen, L. Zhang, Springer International Publishing, Cham, **2017**, pp. 115–123; dd) F. Chen, J. Li, Y. Zhang, D. Yang, Q. Shen, L. Zhang, Springer International Publishing, Cham, **2017**, pp. 115–123; ee) F. Chen, J. Li, Y. Zhang, D. Yang, Q. Shen, L. Zhang, Springer International Publishing, Cham, **2017**, pp. 115–123; ff) F. Chen, J. Li, Y. Zhang, D. Yang, Q. Shen, L. Zhang, Springer International Publishing, Cham, **2017**, pp. 115–123; gg) F. Chen, J. Li, Y. Zhang, D. Yang, Q. Shen, L. Zhang, Springer International Publishing, Cham, **2017**, pp. 115–123; hh) F. Chen, J. Li, Y. Zhang, D. Yang, Q. Shen, L. Zhang, Springer International Publishing, Cham, **2017**, pp. 115–123; ii) F. Chen, J. Li, Y. Zhang, D. Yang, Q. Shen, L. Zhang, Springer International Publishing, Cham, **2017**, pp. 115–123; jj) F. Chen, J. Li, Y. Zhang, D. Yang, Q. Shen, L. Zhang, Springer International Publishing, Cham, **2017**, pp. 115–123; kk) F. Chen, J. Li, Y. Zhang, D. Yang, Q. Shen, L. Zhang, Springer International Publishing, Cham, **2017**, pp. 115–123; ll) F. Chen, J. Li, Y. Zhang, D. Yang, Q. Shen, L. Zhang, Springer International Publishing, Cham, **2017**, pp. 115–123; mm) F. Chen, J. Li, Y. Zhang, D. Yang, Q. Shen, L. Zhang, Springer International Publishing, Cham, **2017**, pp. 115–123; nn) F. Chen, J. Li, Y. Zhang, D. Yang, Q. Shen, L. Zhang, Springer International Publishing, Cham, **2017**, pp. 115–123; oo) F. Chen, J. Li, Y. Zhang, D. Yang, Q. Shen, L. Zhang, Springer International Publishing, Cham, **2017**, pp. 115–123; pp) F. Chen, J. Li, Y. Zhang, D. Yang, Q. Shen, L. Zhang, Springer International Publishing, Cham, **2017**, pp. 115–123; qq) F. Chen, J. Li, Y. Zhang, D. Yang, Q. Shen, L. Zhang, Springer International Publishing, Cham, **2017**, pp. 115–123; rr) F. Chen, J. Li, Y. Zhang, D. Yang, Q. Shen, L. Zhang, Springer International Publishing, Cham, **2017**, pp. 115–123; uu) F. Chen, J. Li, Y. Zhang, D. Yang, Q. Shen, L. Zhang, Springer International Publishing, Cham, **2017**, pp. 115–123; vv) F. Chen, J. Li, Y. Zhang, D. Yang, Q. Shen, L. Zhang, Springer International Publishing, Cham, **2017**, pp. 115–123; ww) F. Chen, J. Li, Y. Zhang, D. Yang, Q. Shen, L. Zhang, Springer International Publishing, Cham, **2017**, pp. 115–123; xx) F. Chen, J. Li, Y. Zhang, D. Yang, Q. Shen, L. Zhang, Springer International Publishing, Cham, **2017**, pp. 115–123; yy) F. Chen, J. Li, Y. Zhang, D. Yang, Q. Shen, L. Zhang, Springer International Publishing, Cham, **2017**, pp. 115–123; zz) F. Chen, J. Li, Y. Zhang, D. Yang, Q. Shen, L. Zhang, Springer International Publishing, Cham, **2017**, pp. 115–123; aa) F. Chen, J. Li, Y. Zhang, D. Yang, Q. Shen, L. Zhang, Springer International Publishing, Cham, **2017**, pp. 115–123; bb) F. Chen, J. Li, Y. Zhang, D. Yang, Q. Shen, L. Zhang, Springer International Publishing, Cham, **2017**, pp. 115–123; cc) F. Chen, J. Li, Y. Zhang, D. Yang, Q. Shen, L. Zhang, Springer International Publishing, Cham, **2017**, pp. 115–123; dd) F. Chen, J. Li, Y. Zhang, D. Yang, Q. Shen, L. Zhang, Springer International Publishing, Cham, **2017**, pp. 115–123; ee) F. Chen, J. Li, Y. Zhang, D. Yang, Q. Shen, L. Zhang, Springer International Publishing, Cham, **2017**, pp. 115–123; ff) F. Chen, J. Li, Y. Zhang, D. Yang, Q. Shen, L. Zhang, Springer International Publishing, Cham, **2017**, pp. 115–123; gg) F. Chen, J. Li, Y. Zhang, D. Yang, Q. Shen, L. Zhang, Springer International Publishing, Cham, **2017**, pp. 115–123; hh) F. Chen, J. Li, Y. Zhang, D. Yang, Q. Shen, L. Zhang, Springer International Publishing, Cham, **2017**, pp. 115–123; ii) F. Chen, J. Li, Y. Zhang, D. Yang, Q. Shen, L. Zhang, Springer International Publishing, Cham, **2017**, pp. 115–123; jj) F. Chen, J. Li, Y. Zhang, D. Yang, Q. Shen, L. Zhang, Springer International Publishing, Cham, **2017**, pp. 115–123; kk) F. Chen, J. Li, Y. Zhang, D. Yang, Q. Shen, L. Zhang, Springer International Publishing, Cham, **2017**, pp. 115–123; ll) F. Chen, J. Li, Y. Zhang, D. Yang, Q. Shen, L. Zhang, Springer International Publishing, Cham, **2017**, pp. 115–123; mm) F. Chen, J. Li, Y. Zhang, D. Yang, Q. Shen, L. Zhang, Springer International Publishing, Cham, **2017**, pp. 115–123; nn) F. Chen, J. Li, Y. Zhang, D. Yang, Q. Shen, L. Zhang, Springer International Publishing, Cham, **2017**, pp. 115–123; oo) F. Chen, J. Li, Y. Zhang, D. Yang, Q. Shen, L. Zhang, Springer International Publishing, Cham, **2017**, pp. 115–123; pp) F. Chen, J. Li, Y. Zhang, D. Yang, Q. Shen, L. Zhang, Springer International Publishing, Cham, **2017**, pp. 115–123; qq) F. Chen, J. Li, Y. Zhang, D. Yang, Q. Shen, L. Zhang, Springer International Publishing, Cham, **2017**, pp. 115–123; rr) F. Chen, J. Li, Y. Zhang, D. Yang, Q. Shen, L. Zhang, Springer International Publishing, Cham, **2017**, pp. 115–123; uu) F. Chen, J. Li, Y. Zhang, D. Yang, Q. Shen, L. Zhang, Springer International Publishing, Cham, **2017**, pp. 115–123; vv) F. Chen, J. Li, Y. Zhang, D. Yang, Q. Shen, L. Zhang, Springer International Publishing, Cham, **2017**, pp. 115–123; ww) F. Chen, J. Li, Y. Zhang, D. Yang, Q. Shen, L. Zhang, Springer International Publishing, Cham, **2017**, pp. 115–123; xx) F. Chen, J. Li, Y. Zhang, D. Yang, Q. Shen, L. Zhang, Springer International Publishing, Cham, **2017**, pp. 115–123; yy) F. Chen, J. Li, Y. Zhang, D. Yang, Q. Shen, L. Zhang, Springer International Publishing, Cham, **2017**, pp. 115–123; zz) F. Chen, J. Li, Y. Zhang, D. Yang, Q. Shen, L. Zhang, Springer International Publishing, Cham, **2017**, pp. 115–123; aa) F. Chen, J. Li, Y. Zhang, D. Yang, Q. Shen, L. Zhang, Springer International Publishing, Cham, **2017**, pp. 115–123; bb) F. Chen, J. Li, Y. Zhang, D. Yang, Q. Shen, L. Zhang, Springer International Publishing, Cham, **2017**, pp. 115–123; cc) F. Chen, J. Li, Y. Zhang, D. Yang, Q. Shen, L. Zhang, Springer International Publishing, Cham, **2017**, pp. 115–123; dd) F. Chen, J. Li, Y. Zhang, D. Yang, Q. Shen, L. Zhang, Springer International Publishing, Cham, **2017**, pp. 115–123; ee) F. Chen, J. Li, Y. Zhang, D. Yang, Q. Shen, L. Zhang, Springer International Publishing, Cham, **2017**, pp. 115–123; ff) F. Chen, J. Li, Y. Zhang, D. Yang, Q. Shen, L. Zhang, Springer International Publishing, Cham, **2017**, pp. 115–123; gg) F. Chen, J. Li, Y. Zhang, D. Yang, Q. Shen, L. Zhang, Springer International Publishing, Cham, **2017**, pp. 115–123; hh) F. Chen, J. Li, Y. Zhang, D. Yang, Q. Shen, L. Zhang, Springer International Publishing, Cham, **2017**, pp. 115–123; ii) F. Chen, J. Li, Y. Zhang, D. Yang, Q. Shen, L. Zhang, Springer International Publishing, Cham, **2017**, pp. 115–123; jj) F. Chen, J. Li, Y. Zhang, D. Yang, Q. Shen, L. Zhang, Springer International Publishing, Cham, **2017**, pp. 115–123; kk) F. Chen, J. Li, Y. Zhang, D. Yang, Q. Shen, L. Zhang, Springer International Publishing, Cham, **2017**, pp. 115–123; ll) F. Chen, J. Li, Y. Zhang, D. Yang, Q. Shen, L. Zhang, Springer International Publishing, Cham, **2017**, pp. 115–123; mm) F. Chen, J. Li, Y. Zhang, D. Yang, Q. Shen, L. Zhang, Springer International Publishing, Cham, **2017**, pp. 115–123; nn) F. Chen, J. Li, Y. Zhang, D. Yang, Q. Shen, L. Zhang, Springer International Publishing, Cham, **2017**, pp. 115–123; oo) F. Chen, J. Li, Y. Zhang, D. Yang, Q. Shen, L. Zhang, Springer International Publishing, Cham, **2017**, pp. 115–123; pp) F. Chen, J. Li, Y. Zhang, D. Yang, Q. Shen, L. Zhang, Springer International Publishing, Cham, **2017**, pp. 115–123; qq) F. Chen, J. Li, Y. Zhang, D. Yang, Q. Shen, L. Zhang, Springer International Publishing, Cham, **2017**, pp. 115–123; rr) F. Chen, J. Li, Y. Zhang, D. Yang, Q. Shen, L. Zhang, Springer International Publishing, Cham, **2017**, pp. 115–123; uu) F. Chen, J. Li, Y. Zhang, D. Yang, Q. Shen, L. Zhang, Springer International Publishing, Cham, **2017**, pp. 115–123; vv) F. Chen, J. Li, Y. Zhang, D. Yang, Q. Shen, L. Zhang, Springer International Publishing, Cham, **2017**, pp. 115–123; ww) F. Chen, J. Li, Y. Zhang, D. Yang, Q. Shen, L. Zhang, Springer International Publishing, Cham, **2017**, pp. 115–123; xx) F. Chen, J. Li, Y. Zhang, D. Yang, Q. Shen, L. Zhang, Springer International Publishing, Cham, **2017**, pp. 115–123; yy) F. Chen, J. Li, Y. Zhang, D. Yang, Q. Shen, L. Zhang, Springer International Publishing, Cham, **2017**, pp. 115–123; zz) F. Chen, J. Li, Y. Zhang, D. Yang, Q. Shen, L. Zhang, Springer International Publishing, Cham, **2017**, pp. 115–123; aa) F. Chen, J. Li, Y. Zhang, D. Yang, Q. Shen, L. Zhang, Springer International Publishing, Cham, **2017**, pp. 115–123; bb) F. Chen, J. Li, Y. Zhang, D. Yang, Q. Shen, L. Zhang, Springer International Publishing, Cham, **2017**, pp. 115–123; cc) F. Chen, J. Li, Y. Zhang, D. Yang, Q. Shen, L. Zhang, Springer International Publishing, Cham, **2017**, pp. 115–123; dd) F. Chen, J. Li, Y. Zhang, D. Yang, Q. Shen, L. Zhang, Springer International Publishing, Cham, **2017**, pp. 115–123; ee) F. Chen, J. Li, Y. Zhang, D. Yang, Q. Shen, L. Zhang, Springer International Publishing, Cham, **2017**, pp. 115–123; ff) F. Chen, J. Li, Y. Zhang, D. Yang, Q. Shen, L. Zhang, Springer International Publishing, Cham, **2017**, pp. 115–123; gg) F. Chen, J. Li, Y. Zhang, D. Yang, Q. Shen, L. Zhang, Springer International Publishing, Cham, **2017**, pp. 115–123; hh) F. Chen, J. Li, Y. Zhang, D. Yang, Q. Shen, L. Zhang, Springer International Publishing, Cham, **2017**, pp. 115–123; ii) F. Chen, J. Li, Y. Zhang, D. Yang, Q. Shen, L. Zhang, Springer International Publishing, Cham, **2017**, pp. 115–123; jj) F. Chen, J. Li, Y. Zhang, D. Yang, Q. Shen, L. Zhang, Springer International Publishing, Cham, **2017**, pp. 115–123; kk) F. Chen, J. Li, Y. Zhang, D. Yang, Q. Shen, L. Zhang, Springer International Publishing, Cham, **2017**, pp. 115–123; ll) F. Chen, J. Li, Y. Zhang, D. Yang, Q. Shen, L. Zhang, Springer International Publishing, Cham, **2017**, pp. 115–123; mm) F. Chen, J. Li, Y. Zhang, D. Yang, Q. Shen, L. Zhang, Springer International Publishing, Cham, **2017**, pp. 115–123; nn) F. Chen, J. Li, Y. Zhang, D. Yang, Q. Shen, L. Zhang, Springer International Publishing, Cham, **2017**, pp. 115–123; oo) F. Chen, J. Li, Y. Zhang, D. Yang, Q. Shen, L. Zhang, Springer International Publishing, Cham, **2017**, pp. 115–123; pp) F. Chen, J. Li, Y. Zhang, D. Yang, Q. Shen, L. Zhang, Springer International Publishing, Cham, **2017**, pp. 115–123; qq) F. Chen, J. Li, Y. Zhang, D. Yang, Q. Shen, L. Zhang, Springer International Publishing, Cham, **2017**, pp. 115–123; rr) F. Chen, J. Li, Y. Zhang, D. Yang, Q. Shen, L. Zhang, Springer International Publishing, Cham, **2017**, pp. 115–123; uu) F. Chen, J. Li, Y. Zhang, D. Yang, Q. Shen, L. Zhang, Springer International Publishing, Cham, **2017**, pp. 115–123; vv) F. Chen, J. Li, Y. Zhang, D. Yang, Q. Shen, L. Zhang, Springer International Publishing, Cham, **2017**, pp. 115–123; ww) F. Chen, J. Li, Y. Zhang, D. Yang, Q. Shen, L. Zhang, Springer International Publishing, Cham, **2017**, pp. 115–123; xx) F. Chen, J. Li, Y. Zhang, D. Yang, Q. Shen, L. Zhang, Springer International Publishing, Cham, **2017**, pp. 115–123; yy) F. Chen, J. Li, Y. Zhang, D. Yang, Q. Shen, L. Zhang, Springer International Publishing, Cham, **2017**, pp. 115–123; zz) F. Chen, J. Li, Y. Zhang, D. Yang, Q. Shen, L. Zhang, Springer International Publishing, Cham, **2017**, pp. 115–123; aa) F. Chen, J. Li, Y. Zhang, D. Yang, Q. Shen, L. Zhang, Springer International Publishing, Cham, **2017**, pp. 115–123; bb) F. Chen, J. Li, Y

- [68] M. Molaei, S. M. Mousavi-Khoshdel, *Comput. Mater. Sci.* **2017**, *139*, 347–353.
- [69] X. Lv, W. Wei, Q. Sun, B. Huang, Y. Dai, *J. Phys. D* **2017**, *50*, 235501.
- [70] W. Song, X. Cao, Z. Wu, J. Chen, K. Huangfu, X. Wang, Y. Huang, X. Ji, *Phys. Chem. Chem. Phys.* **2014**, *16*, 17681–17687.
- [71] K. Hoang, *Phys. Rev. Appl.* **2015**, *3*, 024013.
- [72] L. L. Wong, H. M. Chen, S. Adams, *Phys. Chem. Chem. Phys.* **2015**, *17*, 9186–9193.
- [73] T. Sarkar, P. Kumar, M. D. Bharadwaj, U. Waghmare, *Phys. Chem. Chem. Phys.* **2016**, *18*, 9344–9348.
- [74] Z.-Y. Mao, Y.-P. Sun, K. Scott, *J. Electroanal. Chem.* **2016**, *766*, 107–119.
- [75] T. Watcharathapong, J. T-Thienprasert, P. Barpanda, R. Ahuja, S. Chakraborty, *J. Mater. Chem. A* **2017**, *5*, 21726–21739.
- [76] C. Zheng, B. Radhakrishnan, I.-H. Chu, Z. Wang, S. P. Ong, *Phys. Rev. Appl.* **2017**, *7*, 064003.
- [77] L. Zhao, H. Zhao, Z. Du, N. Chen, X. Chang, Z. Zhang, F. Gao, A. Trencek-Zajac, K. Świernczek, *Electrochim. Acta* **2018**, *282*, 510–519.
- [78] S. Adams, R. Prasada Rao, *J. Mater. Chem.* **2012**, *22*, 7687–7691.
- [79] K. Meier, T. Laino, A. Curioni, *J. Phys. Chem. C* **2014**, *118*, 6668–6679.
- [80] R. Jalem, M. Nakayama, T. Kasuga, *Solid State Ionics* **2014**, *262*, 589–592.
- [81] B. Lang, B. Ziebarth, C. Elsässer, *Chem. Mater.* **2015**, *27*, 5040–5048.
- [82] Y. Deng, C. Eames, J. N. Chotard, F. Lalere, V. Seznec, S. Emge, O. Pecher, C. P. Grey, C. Masquelier, M. S. Islam, *J. Am. Chem. Soc.* **2015**, *137*, 9136–9145.
- [83] S.-H. Bo, Y. Wang, J. C. Kim, W. D. Richards, G. Ceder, *Chem. Mater.* **2015**, *28*, 252–258.
- [84] Y. Noda, K. Nakano, H. Takeda, M. Kotobuki, L. Lu, M. Nakayama, *Chem. Mater.* **2017**, *29*, 8983–8991.
- [85] X. Wang, R. Xiao, H. Li, L. Chen, *Phys. Rev. Lett.* **2017**, *118*, 195901.
- [86] S. Panda, K. Kundu, S. Umapathy, R. L. Gardas, *ChemPhysChem* **2017**, *18*, 3416–3428.
- [87] S. Xue, Y. Liu, Y. Li, D. Teeters, D. W. Crunkleton, S. Wang, *Electrochim. Acta* **2017**, *235*, 122–128.
- [88] B. Singh, M. K. Gupta, R. Mittal, M. Zbiri, S. Rols, S. J. Patwe, S. N. Achary, H. Schober, A. K. Tyagi, S. L. Chaplot, *Phys. Chem. Chem. Phys.* **2017**, *19*, 15512–15520.
- [89] B. Singh, M. K. Gupta, R. Mittal, S. L. Chaplot, *J. Mater. Chem. A* **2018**, *6*, 5052–5064.
- [90] A. Dive, C. Benmore, M. Wilding, S. W. Martin, S. Beckman, S. Banerjee, *J. Phys. Chem. B* **2018**, *122*, 7597–7608.
- [91] T. H. Wan, Z. Lu, F. Ciucci, *J. Power Sources* **2018**, *390*, 61–70.
- [92] F. Chen, R. Kerr, M. Forsyth, *J. Chem. Phys.* **2018**, *148*, 193813.
- [93] P. Prakash, J. Aguirre, M. M. Van Vliet, P. R. Chinnam, D. A. Dikin, M. J. Zdilla, S. L. Wunder, A. Venkatnathan, *J. Mater. Chem. A* **2018**, *6*, 4394–4404.
- [94] S. Panahian Jand, P. Kaghazchi, *MRS Communications* **2018**, *8*, 591–596.
- [95] H. Chen, H. Tu, C. Hu, Y. Liu, D. Dong, Y. Sun, Y. Dai, S. Wang, H. Qian, Z. Lin, L. Chen, *J. Am. Chem. Soc.* **2018**, *140*, 896–899.
- [96] a) P. Lupetin, G. Gregori, J. Maier, *Angew. Chem. Int. Ed.* **2010**, *49*, 10123–10126; *Angew. Chem.* **2010**, *122*, 10321–10324; b) X. Lu, J. W. Howard, A. Chen, J. Zhu, S. Li, G. Wu, P. Dowden, H. Xu, Y. Zhao, Q. Jia, *Adv. Sci.* **2016**, *3*, 1500359; c) S. Li, J. Zhu, Y. Wang, J. W. Howard, X. Lu, Y. Li, R. S. Kumar, L. Wang, L. L. Daemen, Y. Zhao, *Solid State Ionics* **2016**, *284*, 14–19.
- [97] J. A. Dawson, P. Canepa, T. Famprakis, C. Masquelier, M. S. Islam, *J. Am. Chem. Soc.* **2018**, *140*, 7044–7044.
- [98] a) D. Morgan, A. Van der Ven, G. Ceder, *Electrochim. Solid-State Lett.* **2004**, *7*, A30–A32; b) C. Wolverton, A. Zunger, *Phys. Rev. B* **1998**, *57*, 2242–2252; c) J. B. Goodenough, *Solid State Ionics* **1994**, *69*, 184–198; d) H. Buschmann, J. Doelle, S. Berendts, A. Kuhn, P. Bottke, M. Wilkening, P. Heitjans, A. Senyshyn, H. Ehrenberg, A. Lotnyk, V. Duppel, L. Kienle, J. Janek, *Phys. Chem. Chem. Phys.* **2011**, *13*, 19378–19392; e) P. R. Rudolf, A. Clearfield, J. D. Jorgensen, *Solid State Ionics* **1986**, *21*, 213–224; f) A. Kuhn, J. Koehler, B. V. Lotsch, *Phys. Chem. Chem. Phys.* **2013**, *15*, 11620–11622; g) J. L. Fourquet, H. Duroy, M. P. CrozierLopez, *J. Solid State Chem.* **1996**, *127*, 283–294; h) W. Schnick, J. Lucke, *Zeitschrift Fur Anorganische Und Allgemeine Chemie* **1990**, *588*, 19–25.
- [99] S. Lee, S. S. Park, *J. Phys. Chem. C* **2014**, *118*, 12642–12648.
- [100] a) L. J. Miara, S. P. Ong, Y. Mo, W. D. Richards, Y. Park, J.-M. Lee, H. S. Lee, G. Ceder, *Chem. Mater.* **2013**, *25*, 3048–3055; b) S. Ramakumar, L. Satyanarayana, S. V. Manorama, R. Murugan, *Phys. Chem. Chem. Phys.* **2013**, *15*, 11327–11338.
- [101] R. Wagner, G. J. Redhammer, D. Rettenwander, A. Senyshyn, W. Schmidt, M. Wilkening, G. Amthauer, *Chem. Mater.* **2016**, *28*, 1861–1871.
- [102] B. Lang, B. Ziebarth, C. Elsaesser, *Chem. Mater.* **2015**, *27*, 5040–5048.
- [103] A. Martinez-Juarez, C. Pecharroman, J. E. Iglesias, J. M. Rojo, *J. Phys. Chem. B* **1998**, *102*, 372–375.
- [104] N. Kamaya, K. Homma, Y. Yamakawa, M. Hirayama, R. Kanno, M. Yonemura, T. Kamiyama, Y. Kato, S. Hama, K. Kawamoto, A. Mitsui, *Nat. Mater.* **2011**, *10*, 682–686.
- [105] M. C. Paulus, M. F. Graf, P. P. R. M. L. Harks, A. Paulus, P. P. M. Schleker, P. H. L. Notten, R. A. Eichel, J. Granwehr, *J. Magn. Reson.* **2018**, *294*, 133–142.
- [106] C. H. Hu, Z. Q. Wang, Z. Y. Sun, C. Y. Ouyang, *Chem. Phys. Lett.* **2014**, *591*, 16–20.
- [107] Y. Harada, T. Ishigaki, H. Kawai, J. Kuwano, *Solid State Ionics* **1998**, *108*, 407–413.
- [108] H. Moriwake, X. Gao, A. Kuwabara, C. A. J. Fisher, T. Kimura, Y. H. Ikuhara, K. Kohama, T. Tojigamori, Y. Ikuhara, *J. Power Sources* **2015**, *276*, 203–207.
- [109] a) Y. Zhao, L. L. Daemen, *J. Am. Chem. Soc.* **2012**, *134*, 15042–15047; b) A. K. Sagotra, D. Errandonea, C. Cazorla, *Nat. Commun.* **2017**, *8*, 963.
- [110] J. A. Brant, D. M. Massi, N. A. W. Holzwarth, J. H. MacNeil, A. P. Douvalis, T. Bakas, S. W. Martin, M. D. Gross, J. A. Aitken, *Chem. Mater.* **2015**, *27*, 189–196.
- [111] S.-H. Bo, Y. Wang, G. Ceder, *J. Mater. Chem. A* **2016**, *4*, 9044–9053.
- [112] Z. Zhang, E. Ramos, F. Lalere, A. Assoud, K. Kaup, P. Hartman, L. F. Nazar, *Energy Environ. Sci.* **2018**, *11*, 87–93.
- [113] H. Chen, H. Tu, C. Hu, Y. Liu, D. Dong, Y. Sun, Y. Dai, S. Wang, H. Qian, Z. Lin, L. Chen, *J. Am. Chem. Soc.* **2018**, *140*, 896–899.
- [114] a) X. Wang, Z. Yang, C. Wang, D. Chen, R. Li, X. Zhang, J. Chen, M. Xue, *J. Power Sources* **2017**, *369*, 138–145; b) W. Deng, X. Wang, C. Liu, C. Li, M. Xue, R. Li, F. Pan, *ACS Applied Energy Materials* **2018**, *1*, 312–318; c) Z. Yang, H. Liang, X. Wang, X. Ma, T. Zhang, Y. Yang, L. Xie, D. Chen, Y. Long, J. Chen, Y. Chang, C. Yan, X. Zhang, X. Zhang, B. Ge, Z. Ren, M. Xue, G. Chen, *ACS Nano* **2016**, *10*, 755–762; d) X. Wang, D. Chen, Z. Yang, X. Zhang, C. Wang, J. Chen, X. Zhang, M. Xue, *Adv. Mater.* **2016**, *28*, 8645–8650; e) L. Zhang, X. Wang, W. Deng, X. Zang, C. Liu, C. Li, J. Chen, M. Xue, R. Li, F. Pan, *Nanoscale* **2018**, *10*, 958–963; f) W. Deng, X. Wang, C. Liu, C. Li, M. Xue, R. Li, F. Pan, *Nanoscale* **2018**, *10*, 6282–6287; g) C. Li, X. Wang, W. Deng, C. Liu, J. Chen, R. Li, M. Xue, *ChemElectroChem* **2018**, *5*, 3887–3892.
- [115] C. Liu, X. Wang, W. Deng, C. Li, J. Chen, M. Xue, R. Li, F. Pan, *Angew. Chem. Int. Ed. Engl.* **2018**, *57*, 7046–7050.
- [116] L. A. Montoro, J. M. Rosolen, *Electrochim. Acta* **2004**, *49*, 3243–3249.
- [117] M. Brighi, P. Schouwink, Y. Sadikin, R. Cerny, *J. Alloys Compd.* **2016**, *662*, 388–395.
- [118] D. O. Shin, K. Oh, K. M. Kim, K.-Y. Park, B. Lee, Y.-G. Lee, K. Kang, *Sci. Rep.* **2015**, *5*, 18053.
- [119] C. Subbu, S. Rajendran, K. Kesavan, C. M. Mathew, *Int. Polym. Process.* **2015**, *30*, 476–486.
- [120] N. Iranipour, D. J. Gunzelmann, A. J. Seeber, J. Vongsivut, A. F. Hollenkamp, M. Forsyth, P. C. Howlett, *J. Mater. Chem. A* **2017**, *5*, 24909–24919.
- [121] a) Q. Cao, H. P. Zhang, G. J. Wang, Q. Xia, Y. P. Wu, H. Q. Wu, *Electrochim. Commun.* **2007**, *9*, 1228–1232; b) F. Gao, Z. Tang, *Electrochim. Acta* **2008**, *53*, 5071–5075.
- [122] a) Y. Tominaga, K. Yamazaki, *Chem. Commun.* **2014**, *50*, 4448–4450; b) S. Das, A. Ghosh, *J. Appl. Phys.* **2015**, *117*, 174103; c) S. Delacroix, F. Sauvage, M. Reynaud, M. Deschamps, S. Bruyere, M. Becuwe, D. Postel, J.-M. Tarascon, N. Albert Nguyen Van, *Chem. Mater.* **2015**, *27*, 7926–7933.
- [123] Y. S. Choi, Y.-S. Lee, K. H. Oh, Y. W. Cho, *Phys. Chem. Chem. Phys.* **2016**, *18*, 22540–22547.
- [124] U. H. Choi, S. Liang, M. V. O'Reilly, K. I. Winey, J. Runt, R. H. Colby, *Macromolecules* **2014**, *47*, 3145–3153.
- [125] X. Fu, C. Li, Y. Wang, L. P. Kovatch, L. Scudiero, J. Liu, W. Zhong, *ACS Appl. Mater. Interfaces* **2018**, *10*, 4726–4736.
- [126] a) Z. Wang, L. Zhou, X. W. Lou, *Adv. Mater.* **2012**, *24*, 1903–1911; b) J. S. Chen, L. A. Archer, X. W. Lou, *J. Mater. Chem.* **2011**, *21*, 9912–9924; c) Y. Zhao, X. Li, B. Yan, D. Xiong, D. Li, S. Lawes, X. Sun, *Adv. Energy Mater.* **2016**, *6*, 1502175.
- [127] J. Zhou, L. Wang, M. Yang, J. Wu, F. Chen, W. Huang, N. Han, H. Ye, F. Zhao, Y. Li, Y. Li, *Adv. Mater.* **2017**, *29*, 1702061.
- [128] F. Niu, J. Yang, N. Wang, D. Zhang, W. Fan, J. Yang, Y. Qian, *Adv. Funct. Mater.* **2017**, *27*, 1700522.

- [129] J. Yuan, C. Chen, Y. Hao, X. Zhang, B. Zou, R. Agrawal, C. Wang, H. Yu, X. Zhu, Y. Yu, Z. Xiong, Y. Luo, H. Li, Y. Xie, *J. Alloys Compd.* **2017**, *691*, 34–39.
- [130] D. Yuan, G. Huang, D. Yin, X. Wang, C. Wang, L. Wang, *ACS Appl. Mater. Interfaces* **2017**, *9*, 18178–18186.
- [131] Q. Li, L. Li, K. A. Owusu, W. Luo, Q. An, Q. Wei, Q. Zhang, L. Mai, *Nano Energy* **2017**, *41*, 109–116.
- [132] a) X. Du, H. Zhao, Y. Lu, Z. Zhang, A. Kulka, K. Swierczek, *Electrochim. Acta* **2017**, *228*, 100–106; b) Z.-Z. Luo, Y. Zhang, C. Zhang, H. T. Tan, Z. Li, A. Abutaha, X.-L. Wu, Q. Xiong, K. A. Khor, K. Hippalgaonkar, J. Xu, H. H. Hng, Q. Yan, *Adv. Energy Mater.* **2017**, *7*, 1601285.
- [133] C. Teng, D. Xie, J. Wang, Z. Yang, G. Ren, Y. Zhu, *Adv. Funct. Mater.* **2017**, *27*, 1700240.
- [134] Y. Yang, J. Li, D. Chen, J. Zhao, *J. Electrochem. Soc.* **2017**, *164*, A6001–A6006.
- [135] X. Tu, Y. Zhou, Y. Song, *Appl. Surf. Sci.* **2017**, *400*, 329–338.
- [136] E. Wang, W. Xiang, R. Rajagopalan, Z. Wu, J. Yang, M. Chen, B. Zhong, S. X. Dou, S. Chou, X. Guo, Y.-M. Kang, *J. Mater. Chem. A* **2017**, *5*, 9833–9841.
- [137] M. Xue, D. Chen, X. Wang, J. Chen, G. F. Chen, *J. Mater. Chem. A* **2015**, *3*, 7715–7718.
- [138] a) J. Ren, Y. Zhang, W. Bai, X. Chen, Z. Zhang, X. Fang, W. Weng, Y. Wang, H. Peng, *Angew. Chem. Int. Ed. Engl.* **2014**, *53*, 7864–7869; b) Z. Guo, Y. Zhao, Y. Ding, X. Dong, L. Chen, J. Cao, C. Wang, Y. Xia, H. Peng, Y. Wang, *Chem* **2017**, *3*, 348–362; c) Z. Zhang, L. Wang, Y. Li, Y. Wang, J. Zhang, G. Guan, Z. Pan, G. Zheng, H. Peng, *Adv. Energy Mater.* **2017**, *7*.
- [139] W. Luo, Y. Gong, Y. Zhu, Y. Li, Y. Yao, Y. Zhang, K. Fu, G. Pastel, C.-F. Lin, Y. Mo, E. D. Wachsman, L. Hu, *Adv. Mater.* **2017**, *29*, 1606042.
- [140] C. Wang, Y. Gong, B. Liu, K. Fu, Y. Yao, E. Hitz, Y. Li, J. Dai, S. Xu, W. Luo, E. D. Wachsman, L. Hu, *Nano Lett.* **2017**, *17*, 565–571.
- [141] L. Fan, H. L. Zhuang, L. Gao, Y. Lu, L. A. Archer, *J. Mater. Chem. A* **2017**, *5*, 3483–3492.
- [142] B. Qiu, M. Zhang, L. Wu, J. Wang, Y. Xia, D. Qian, H. Liu, S. Hy, Y. Chen, K. An, Y. Zhu, Z. Liu, Y. S. Meng, *Nat. Commun.* **2016**, *7*, 12108.
- [143] V. Thangadurai, S. Narayanan, D. Pinzar, *Chem. Soc. Rev.* **2014**, *43*, 4714–4727.
- [144] W. Zhou, S. Wang, Y. Li, S. Xin, A. Manthiram, J. B. Goodenough, *J. Am. Chem. Soc.* **2016**, *138*, 9385–9388.
- [145] R. H. Basappa, T. Ito, H. Yamada, *J. Electrochem. Soc.* **2017**, *164*, A666–A671.
- [146] a) Y. Yamada, K. Furukawa, K. Sodeyama, K. Kikuchi, M. Yaegashi, Y. Tateyama, A. Yamada, *J. Am. Chem. Soc.* **2014**, *136*, 5039–5046; b) J. Guo, Z. Wen, M. Wu, J. Jin, Y. Liu, *Electrochim. Commun.* **2015**, *51*, 59–63.
- [147] a) J.-Z. Kong, S.-S. Wang, G.-A. Tai, L. Zhu, L.-G. Wang, H.-F. Zhai, D. Wu, A.-D. Li, H. Li, *J. Alloys Compd.* **2016**, *657*, 593–600; b) D. Guan, L. Ma, D. Pan, J. Li, X. Gao, Y. Xie, M. Qiu, C. Yuan, *Electrochim. Acta* **2017**, *242*, 117–124.
- [148] a) C. M. Park, J. H. Kim, H. Kim, H. J. Sohn, *Chem. Soc. Rev.* **2010**, *39*, 3115–3141; b) N. Liu, Z. D. Lu, J. Zhao, M. T. McDowell, H. W. Lee, W. T. Zhao, Y. Cui, *Nat. Nanotechnol.* **2014**, *9*, 187–192.
- [149] a) M. Sathiya, K. Ramesha, G. Rousse, D. Foix, D. Gonbeau, A. S. Prakash, M. L. Doublet, K. Hemalatha, J. M. Tarascon, *Chem. Mater.* **2013**, *25*, 1121–1131; b) M. Oishi, C. Yogi, I. Watanabe, T. Ohta, Y. Orikasa, Y. Uchimoto, Z. Ogumi, *J. Power Sources* **2015**, *276*, 89–94; c) H. Koga, L. Croguennec, M. Ménétrier, P. Mannessiez, F. Weill, C. Delmas, *J. Power Sources* **2013**, *236*, 250–258.

Manuscript received: December 18, 2018

Revised manuscript received: March 15, 2019

Version of record online: April 5, 2019